DEVELOPMENT OF A LABORATORY EXAFS FACILITY AND ITS

APPLICATION TO AMORPHOUS AND CRYSTALLINE

GERMANIUM

by

Muhammad Hikam

B. Sc., University of Indonesia, 1981

Drs., University of Indonesia, 1983

A THESIS SUBMITTED IN PARTIAL FULFILLMENT OF

THE REQUIREMENTS FOR THE DEGREE OF

MASTER OF SCIENCE

in the Department

of

Physics

© Muhammad Hikam 1987

SIMON FRASER UNIVERSITY

July 1987

APPROVAL

Name: Muhammad Hikam

Degree: Master of Science

Title of Thesis: Development of a Laboratory EXAFS facility and
                 its Application to Amorphous and Crystalline
                 Germanium

Examining Committee:

  Chairman: Dr. J. F. Cochran

  Dr. E. D. Crozier
  Senior Supervisor

  Dr. R. H. Enns

  Dr. R. F. Frindt

  Dr. S. Gygax

  Examiner
  Professor
  Department of Physics
  Simon Fraser University

                 Date Approved: July 17, 1987

PARTIAL COPYRIGHT LICENSE

I hereby grant to Simon Fraser University the right to lend my thesis, project or extended essay (the title of which is shown below) to users of the Simon Fraser University Library, and to make partial or single copies only for such users or in response to a request from the library of any other university, or other educational institution, on its own behalf or for one of its users. I further agree that permission for multiple copying of this work for scholarly purposes may be granted by me or the Dean of Graduate Studies. It is understood that copying or publication of this work for financial gain shall not be allowed without my written permission.

Title of Thesis/Project/Extended Essay

Development of a Laboratory EXAFS Facility and its Application

to Amorphous and Crystalline Germanium

Author:

(signature)

·Muhammad Hikam

(name)

Sept 15, 1987

(date)

ABSTRACT

An EXAFS (Extended X-ray Absorption Fine Structure) spectrometer
has been constructed. The spectrometer is equipped with a curved
crystal monochromator to focus and select the energy of the
x-rays. Utilizing a sealed-tube x-ray generator and Johann-type
monochromator crystal, photon fluxes between 10^4 and 10^5
photons/sec are achieved in the energy range between 5 and 20 KeV.
The energy resolution at 11 keV is 14 eV.

The EXAFS spectra of Ge in amorphous and crystalline states are
measured with this system, and are compared with results from SSRL
(Stanford Synchrotron Radiation Laboratory) data. The nearest
neighbour interatomic distance obtained in the experiment has good
agreement with the known distance, for both amorphous and
crystalline germanium.

TABLE OF CONTENTS

List of Tables

List of Figures

Chapter 1

INTRODUCTION

Extended x-ray absorption fine structure (EXAFS) has proven to be a useful tool for structural studies. As a probe of local structure it has many advantages for obtaining information about complex systems and has been used in investigation of, for instance, amorphous materials, catalysts, and surface and biological systems [Lee *et al.*, 1981; Hayes and Boyce, 1982].

The phenomenon of extended x-ray absorption fine structure refers to the oscillation of the x-ray absorption coefficient as a function of x-ray energy above the threshold. Such oscillation can extend up to 2000 eV above the edge and may have a magnitude of 10% or more relative to the absorption at the edge.

The absorption spectrum near the K-edge in crystalline Ge is shown in Fig. 1.1. The oscillation in the absorption may be interpreted in a quantitative way in terms of the scattering of the excited photoelectrons by the neighbouring atoms and the resulting interference of the reflected electron wave with the outgoing photoelectron waves.

1
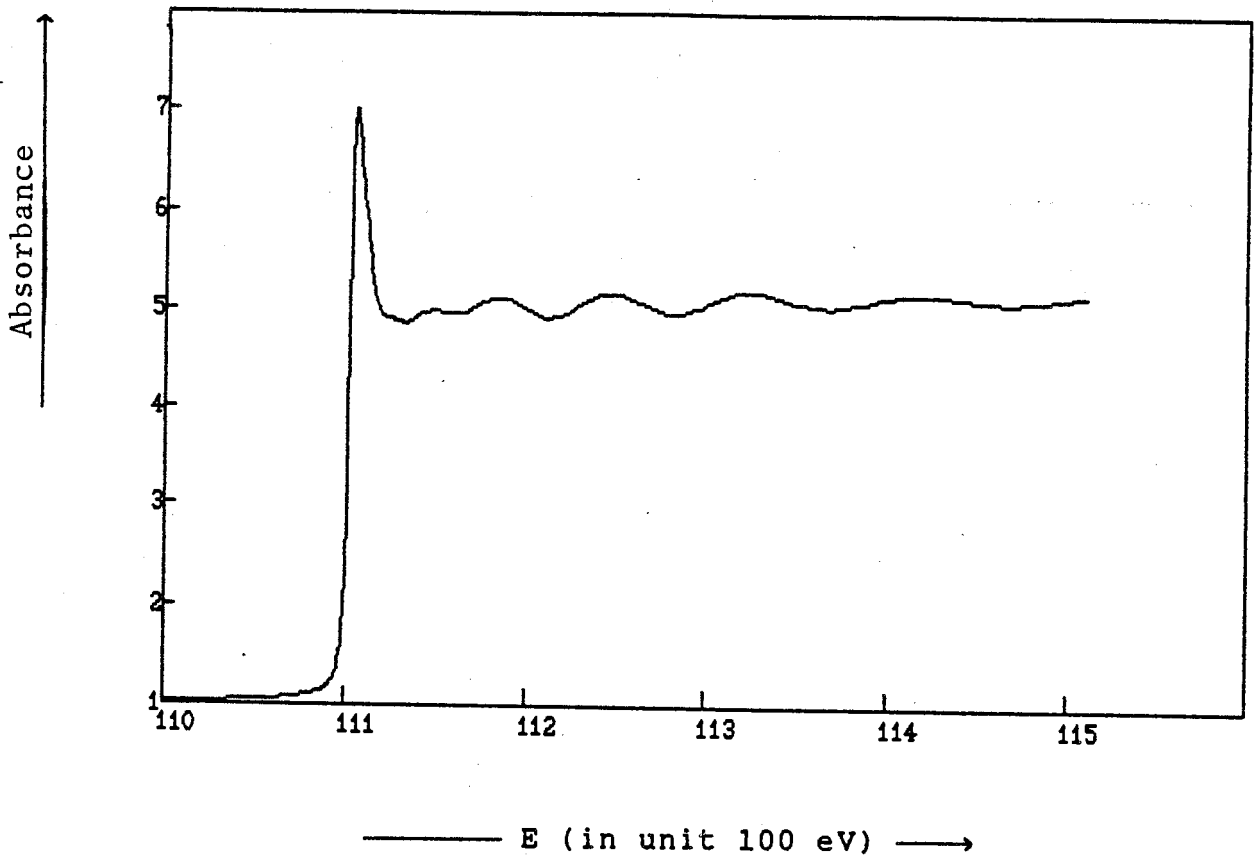
Fig. 1.1: *X-ray absorption spectrum of crystalline Ge, measured at SSRL.*

The oscillatory part of the absorption coefficient, $\Delta\mu$, normalized to the structureless background μ_o is defined in the simplest approximation by [Sayers *et al.*, 1971; Lee *et al.*, 1981]

$$\chi(k) = \frac{\Delta \mu}{\mu_o}$$

$$= \sum_j \frac{N_j}{kR^2_j} S^2_o(k) |f_j(k,\pi)| \sin \{2k R_j + \delta_j(k)\} \times$$

$$e^{-2\sigma^2_j k^2} e^{-2R_j/\lambda_j(k)} \tag{1.1}$$

Equation (1.1) describes the modifications of the photoelectron wave function at the origin due to scattering by N_j neighbours located a radial distance of R_j away. This is illustrated in Fig. 1.2 where an outgoing wave is shown backscattered by a neighbouring atom; $f_j(k,\pi)$ is the backscattering amplitude. The photoelectron wavevector k is defined as

$$k = \hbar^{-1}[2m(\hbar\omega - E_o)]^{1/2}, \tag{1.2}$$

where $\hbar\omega$ is the x-ray energy and E_o is the threshold energy for absorption. The electron wave will be phase-shifted by $2kr_j$ by the time it makes the return trip to the neighbour. To this one must add $\delta_j(k)$, the sum of the phase change due to the backscattering process and the phase change as the photoelectron leaves and returns to the potential of the x-ray absorbing atom. In addition, one has to account for the fact that the atoms are not stationary; in the harmonic approximation this can be accounted for by a Debye-Waller term $e^{-2k^2\sigma^2_j}$, where σ^2_j is the mean square relative displacement between the scattering and absorbing atoms. $S^2_o(k)$ is

3
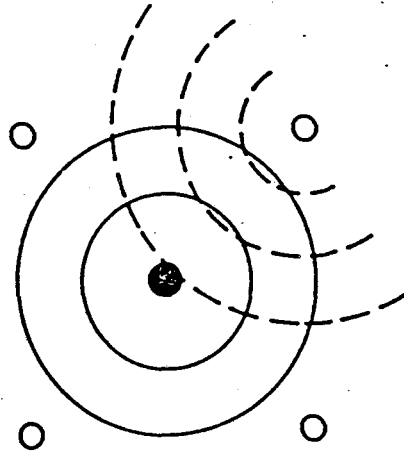
Fig 1.2 : *Outgoing photoelectron waves (solid lines) propagate to neighbouring atoms represented by open circles. The backscattered waves (dashed lines) modify the wave function at the central atom and give rise to EXAFS.*

the correction for many-body effects. Finally one has also to take into account that electrons that have suffered inelastic losses will not have the right wavevector to contribute to the interference process; this is crudely accounted for by an exponential damping term $e^{-2R_j/\lambda}$, where λ is the inelastic electron mean free path.

4

In deriving equation (1.1) several assumptions are made, *i.e.* EXAFS is short-range (only the environment of the excited atom is responsible for EXAFS), only a single electron is excited, multiple scattering is neglected, and the harmonic solid approximation is used (which is equivalent to assuming that the distribution of atoms about the x-ray absorbing atom is Gaussian). Equation (1.1) is a valid approximation for some amorphous films, glasses and liquids in which a high degree of local order is preserved by covalent bonding or a strong ion-ion interaction [Crozier *et al.*, 1987]. But frequently the degree of disorder is larger and $\chi(k)$ must be represented by the more general equation [Stern, 1974; Crozier and Seary, 1980; Brown and Doniach, 1980]:

$$\chi(k) = \sum_{j} S_o^2(k) \left| f_j(k,\pi) \right| \int \frac{P(R_j)}{kR_j^2} \sin \{ 2k\, R_j + \delta_j(k) \}\ \mathrm{x}$$

$$e^{-2R_j/\lambda_j(k)} \, dR_j. \tag{1.3}$$

where $P(R_j)$ is the probability of finding the j-th species in the range R_j to $R_j + dR_j$.

By using a Fourier transform, Sayers *et al.* [1971] show how to invert equation (1.1), to obtain a model structure function which contains information on the number, distance to and distribution

5

of atoms surrounding the absorbing atom.

The amplitude of EXAFS oscillations is small compared with the total absorption background (about 10% for pure elements, and less than 1% for dilute systems); therefore, EXAFS analysis requires high-accuracy absorption spectra. Synchrotron radiation is the most suitable radiation source because of its properties of high photon flux, small beam divergence, structureless spectrum, and nearly linear polarization state.

Synchrotron radiation, using a double crystal monochromator with flat crystals, can provide significantly good resolution. The energy resolution, ΔE, currently available in the hard x-ray regime at a synchrotron radiation source is $\Delta E \simeq 10^{-4}$ E, where E is the x-ray energy. Such resolution offers the possibility of determining accurate coordination numbers since it allows for obtaining better information about second and more distant neighbours. The high resolution also allows the accurate measurement and utilization of edge and near-edge structure to gain a better understanding of the structure of the material.

Increasing interest in synchrotron radiation, however, leads to restrictions in access to it. Therefore, the use of laboratory facilities for EXAFS studies on moderately concentrated samples, which do not make extremely high demands on photon flux, is essential [Stern, 1980].

A severe limitation of a synchrotron radiation source is that time on the source is so precious that there is great pressure to measure as much as feasible because one will not be able to use the source again for several months. Under such conditions, any new ideas that come up while doing an experiment can not be implemented immediately. In a laboratory facility one can have continuous interactive innovation with the apparatus, one can think over an experimental setup and gain better understanding in the process.

The purpose of this thesis is to describe an EXAFS system that has been developed in our laboratory at SFU. The facility is based on a focussing crystal monochromator, and uses the Bremsstrahlung radiation from a sealed-tube x-ray generator. Under the control of a PDP 11/34 computer the output x-ray energy of the monochromator is varied and an x-ray absorption spectrum digitally obtained. This system provides photon fluxes of 10^3-10^5 photons/second over the energy range 5 - 20 KeV; at 11 keV, the energy resolution is 14 eV. The system may provide photon fluxes of 10^6 photons/sec with the correct choice of a monochromator crystal and optimal bending of the crystal. This would also improve the energy resolution to 5 eV at 11 keV [Thulke *et al.*, 1983].

We begin, in chapter 2, with a general description of this EXAFS laboratory. First, we compare synchrotron radiation and sealed-

tube x-ray generator sources. A discussion of flat and curved crystal monochromators is in the next section. This chapter also describes the spectrometer configuration used in this thesis, *i.e.* Rowland circle and arrangement of source, crystal and sample. Several types of detectors with emphasis on ionization detectors, which we use here, are discussed. Consideration of radiation hazards and safety is included in the chapter. The setup procedure and alignment is discussed at the end of the chapter.

Chapter 3 discusses the automation of the system. Hardware and software considerations of the system are discussed briefly. This chapter also contains a short description of EXAFS analysis.

Chapter 4 discusses the performance of the facility. It examines the data collection. Intensity and energy resolution as the result of the experiment are discussed, followed by consideration of the limitations of the equipment, and other types of experiments that can be done using the equipment.

An application of this system to crystalline and amorphous Ge samples is given in chapter 5. The results are analysed and compared with data obtained at SSRL (Stanford Synchrotron Radiation Laboratory).

In the final chapter we summarize our work and draw some conclusions from the results and discuss further development of the system.

Chapter 2

EXPERIMENTAL TECHNIQUES

An EXAFS spectrum can be derived from a measurement of the photo cross section over an appropriate range of x-ray energy. The basic apparatus to measure an EXAFS spectrum consists of an x-ray source, a monochromator to select energy, and detectors.

2.1. Source

Two sources of continuous x-ray radiation are available for EXAFS experiments: Bremsstrahlung from a conventional x-ray source and synchrotron radiation produced by electron storage rings.

In an x-ray tube, x-rays are produced when high-energy electrons strike the anode. The spectrum consists of both continuous Bremsstrahlung radiation and characteristic line spectra. The characteristic lines are more intense than the continuous radiation. In an EXAFS scan, the continuous radiation is used; strong characteristic emission lines can severely distort the EXAFS spectrum if they lie in the range of the scan.

Synchrotron radiation is produced by electrons or other charged particles travelling at relativistic velocities in curved orbits in a storage ring [Winick, 1980]. Synchrotron radiation has very high intensity: in SSRL running at 3 GeV and using a mirror to collect 6 mrad of horizontal divergence, about 10^{11} photons/sec eV are obtained in the 7 keV energy region.

In our laboratory, the x-rays are generated by a water-cooled sealed tube, Elliott Marconi 315-TX, with tungsten target. The accelerating voltage of the Picker x-ray generator can be varied from 15 to 50 kVolts with tube current up to 45 mA. The size of the x-ray source is 10 mm x 1 mm (normal focus).

2.2. Monochromators

One way to monochromatize an x-ray beam is by diffraction from a crystal. In our laboratory, a bent crystal monochromator is used. In addition to that, a bent crystal also focuses the source's diverging radiation on the sample, with a resulting increase in intensity (but with some loss in energy resolution).

One can determine what kind of curvature of bent crystal to use in focusing the x-rays by looking at these two conditions:

1. From the Bragg condition: the angles of incidence and reflection waves referred to the reflecting atomic planes must be

equal at all points on the surface.

2. In order to have monoenergetic x-rays, the angle of deviation ψ of the reflected x-ray must be constant and equal to:

$$\psi = 2 \arcsin (m \lambda/2d), \qquad (2.1)$$

where $\psi = 2\theta$ (see Fig. 2.1)
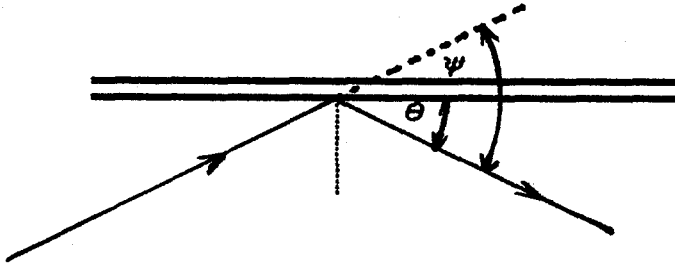
Fig. 2.1: *Bragg diffraction.*

Condition (1) dictates the direction of the curve at every point, while condition (2) dictates the position of each point on the curve.

It is easy to see that the two conditions are incompatible, by noting that condition (2) is satisfied if, and only if, the curve is a circular arc through S and F (see Fig. 2.2), of radius R, where

$$R = \overline{SF}/(2 \sin \psi),$$

whereas condition (1) is not satisfied by this solution.
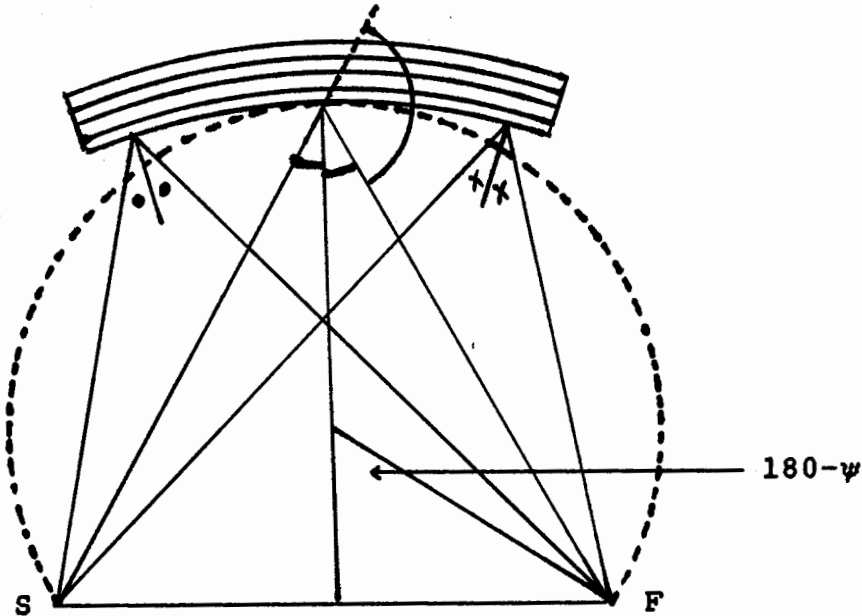
Fig. 2.2: *To illustrate the impossibility of satisfying both conditions for Bragg reflection with a bent crystal over an extended surface if the atomic reflecting planes coincide with the reflecting boundary of the crystal, and if focusing at F from source S is required.*

However, the two conditions mentioned above do not have to be imposed on the same surface, so that one can arrange a geometry such that both conditions are met (see Fig. 2.3). In this case the atomic reflecting planes and the boundary surface of the crystal are not parallel.
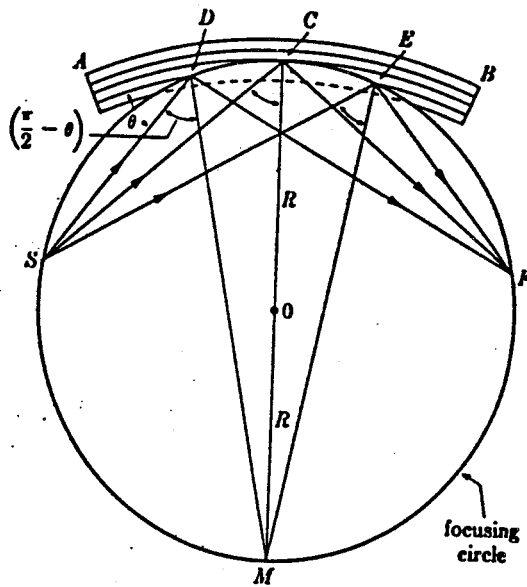
Fig. 2.3: *Rowland Geometry. A line source of x-rays, the focal line on the tube target, is located at S perpendicular to the plane of drawing. The crystal AB is in the form of a rectangular plate and has a set of reflecting planes parallel to its surface. It is bent into a circular form so that the radius of curvature of the plane through C is 2R =* $\overline{CM}$*; in this way, all the plane normals are made to pass through M , which is located on the same circle, of radius R, as the source S (assuming that the Bragg planes remain parallel when the crystal is bent). If the face of the crystal is then cut away behind the dotted line to a radius of R, then all rays diverging from the source S will encounter the lattice planes at the same Bragg angle, since the angles SDM, SCM, and SEM are all equal to one another, being inscribed on the same arc SM, and have the value* $(\pi/2 - \theta)$*.*

14

The boundary of the crystal coincides with part of the circle at centre O with radius R, called the Rowland radius. The atomic reflecting planes of this crystal are bent so that they coincide with concentric circles centered on the circumference of circle O (radius 2R).

From Fig. 2.3 the two conditions can be satisfied. The angles of incident and reflected waves are the same at all points, and the angles of the deviation of the beam are constant. This arrangement is called the Rowland geometry, and the crystal cut in this fashion is called a Johansson-cut crystal [Cullity, 1978].

A precise Johansson-cut crystal is not easily achieved: the crystal is bent at radius 2R at first, and then it is ground so that the surface has radius R.

One can consider another arrangement by noting that condition (2) above, fixing the position of the boundary of the crystal, is less stringent than condition (1), fixing the direction of the atomic planes. If the arc of the focal circle covered by the crystal is not too large (or in other words the dimension of the crystal is small compared with the radius of a Rowland circle), the aberrations of focusing can be kept sufficiently small for practical purposes without requiring the difficulty of curved profiling of the boundary surface [DuMond, 1947]. Such an

15

arrangement in which a crystal is bent with radius twice Rowland circle radius is called a Johann-cut crystal.

The following figures (Fig 2.4) show the comparison between Johann and Johansson cut.

a.

b.
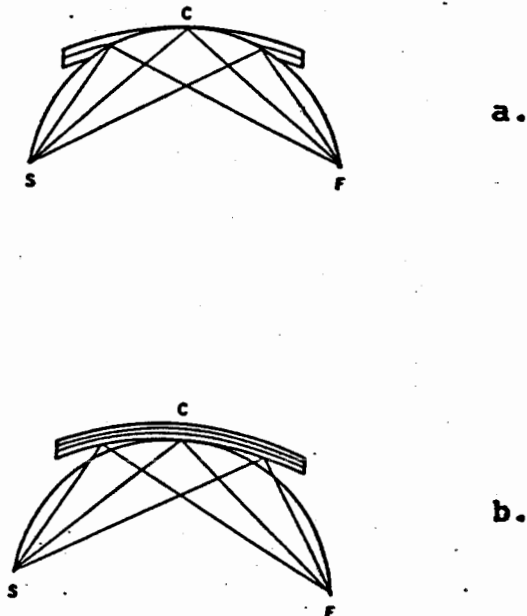
Fig. 2.4. a) Johansson-cut crystal

b) Johann-cut crystal

It is found that the reflectivity of the Johann crystal arrangement is relatively comparable to that of the Johansson [Lu

16

and Stern, 1980]. The Johansson crystal is 1.5 - 3.4 times more intense than the Johann crystal. The intensity gain in using a bent crystal over a plane crystal is substantial (200 - 300 times) and clearly worthwhile.
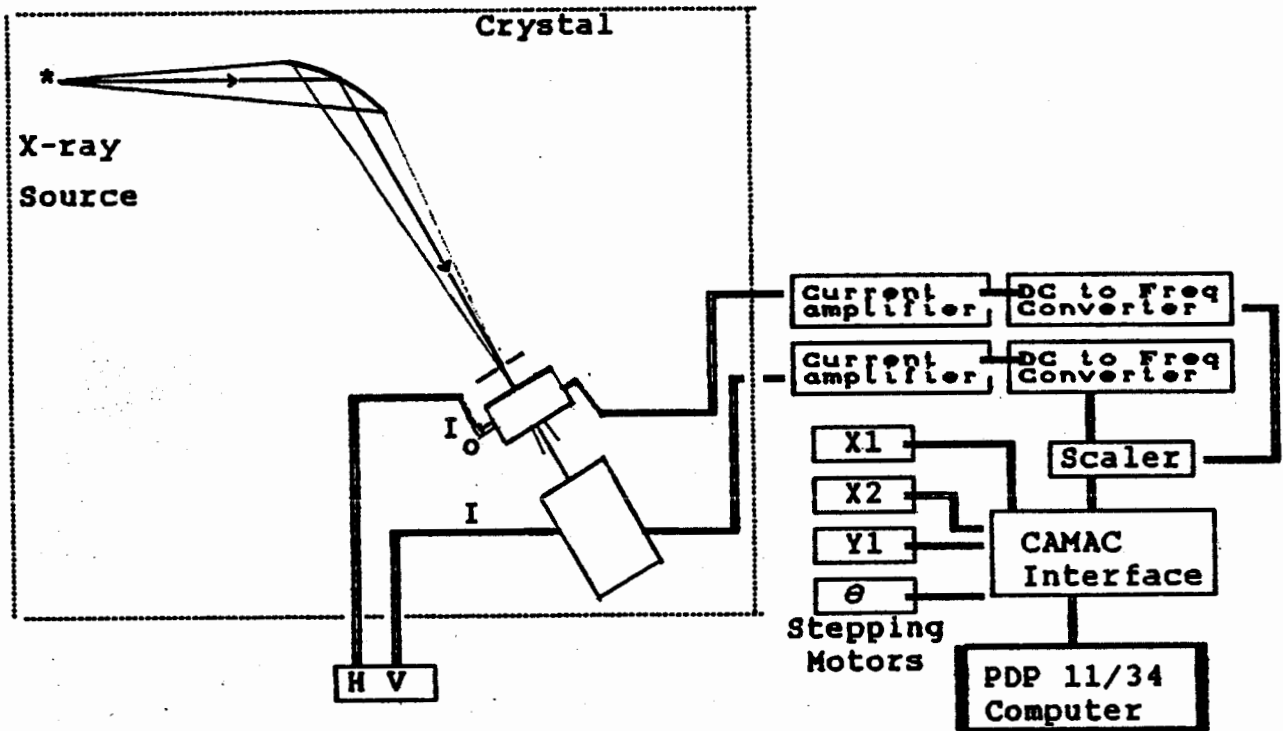
Fig. 2.5: *Schematic diagram of EXAFS spectrometer.*

Since the conference on laboratory EXAFS facilities and their relation to Synchrotron Radiation Source at Washington State University, Seattle, in April 1980, many new techniques and technologies have been developed and new laboratory EXAFS

17

facilities have been built and published in the literature [Cohen et al., 1980; Georgopoulos and Knapp, 1981; Khalid et al., 1982; Maeda et al., 1982; Cohen and Deslattes, 1982; Thulke et al., 1983; Williams, 1983; Tohji and Udagawa, 1983; Ito and Iwasaki, 1983; Kawasaki and Udagawa, 1983]. A schematic diagram of the focusing EXAFS system (based on the designed by Thulke et al., 1983) is shown in Fig. 2.5.

A Johann cut crystal monochromatizes and collects the x-ray beam from the source and focusses it on the exit slit. The specimen is placed after the exit slit between two detectors which monitor the incident beam intensity I_o and the transmitted photon flux I. The detectors are ionization chambers. The ionization currents are amplified and converted to frequencies. The signals from the first and second ionization chambers are counted until inhibited by the timer. After readout, the spectrometer is set to the next incremental energy, and both counters are started again. The data of the spectra are stored on a diskette on the PDP-11/34 computer which also controls the motion of the spectrometer. Further details of the hardware and software are given in chapter 3.

The position of the source and the direction of the primary beam are stationary. Varying the energy of the photons requires rotating and translating the crystal, and moving the exit slit to keep track of the beam such that the source, crystal and exit slit lie on the arc of the Rowland circle (Fig. 2.6). Let the source be

18

the origin of an orthogonal system of coordinates (x,y), where x is in the direction of the primary beam. Letting x_c be the distance between source and crystal, from geometry x_c has to satisfy the following equation

$$x_c = 2 \, R \, \text{Sin} \, \theta_B, \qquad (2.2)$$
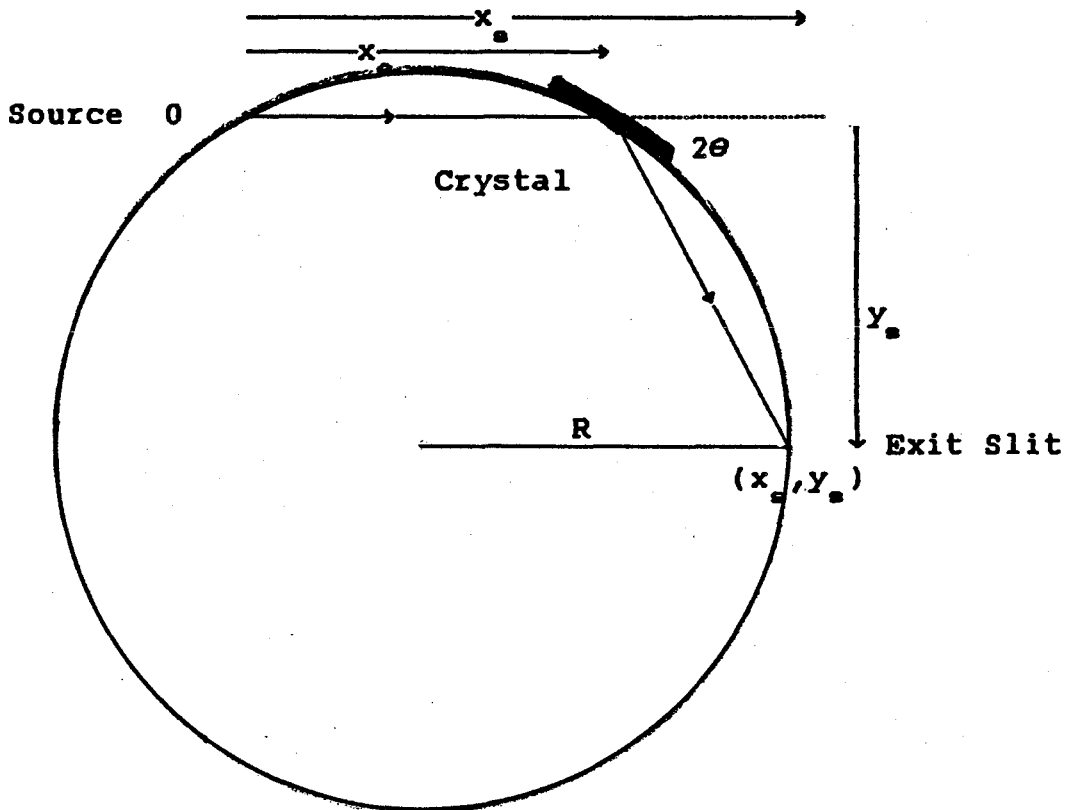
Fig. 2.6: Geometry of the monochromator based on a Johann-cut crystal. The coordinates of the crystal center and the exit slit are $(x_c, 0)$ and (x_s, y_s) respectively. R is the focusing circle radius.

where θ_B is the Bragg angle. The exit slit is aligned on the Rowland circle at the same distance as that between source and crystal. The position of the exit slit is given by

$$x_s = x_c + x_c \cos 2\theta_B, \qquad (2.3)$$

$$y_s = x_c \sin 2\theta_B \qquad (2.4)$$

In practice, the exit slit is placed at a finite distance L from the centre of the sample translation stage (see Fig. 2.7), so the position of the centre of the sample translation stage is given by

$$x_1 = (x_c + L) \cos 2\theta_B, \qquad (2.5)$$

$$y_1 = (x_c + L) \sin 2\theta_B, \qquad (2.6)$$

where L was measured by a vernier caliper to be 88.247 ± 0.01 mm, x_c is redefined to be x_2, and (x_1, y_1) are the coordinates of the center of the sample translation stage with the crystal as origin.

The choice of the crystal size and of its bending radius is a compromise between gain of intensity and loss of resolution. The width of the crystal determines the minimum bending radius which is necessary to gain maximum monochromatic intensity; however, the energy resolution decreases with decreasing crystal bending radius.
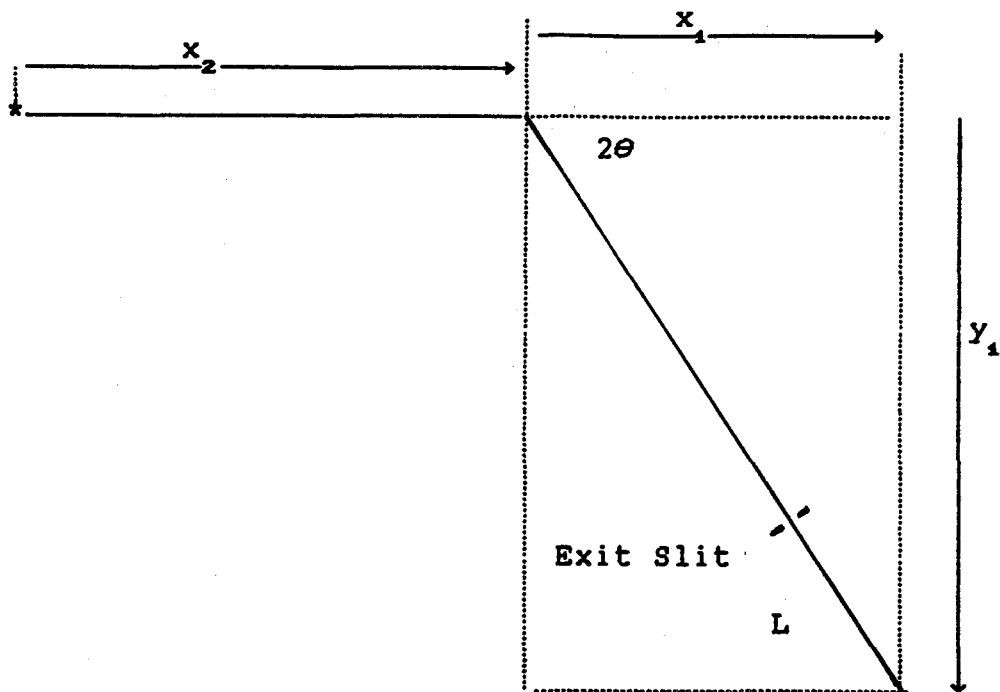
Fig. 2.7: *The exit slit position.*

In our laboratory, we use a 60 mm wide and 20 mm high Si(111) Johann-type crystal with the radius of Rowland circle 354 ± 5 mm. Due to the bending scheme, the area of the crystal exposed to x-rays is 40 mm x 20 mm.

2.3. Construction of the Spectrometer

Fig. 2.8 shows the EXAFS spectrometer that we built at Simon Fraser University. The spectrometer consists of a single-axis goniometer and three translation stages, shown schematically in

Fig. 2.9. The crystal (CRYS) is turned by the goniometer (GON) which is attached to the sliding motor of the lower stage (SM1). This lower slide moves the goniometer according to equation (2.2) and at the same time moves the other two stages (SM2 and SM3). Stages SM2 and SM3 move the detector platform (PLAT) such that the centre of PLAT is at the position specified by equations (2.5) and (2.6).
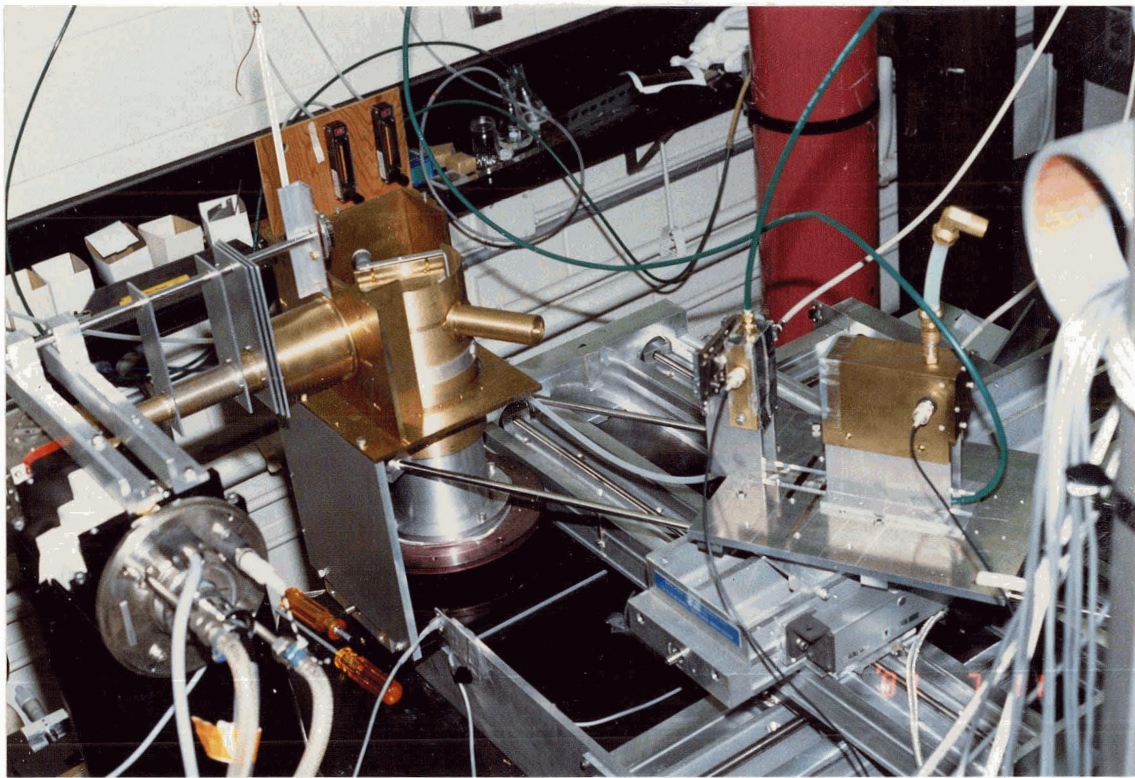
Fig. 2.8: *The EXAFS spectrometer at SFU.*
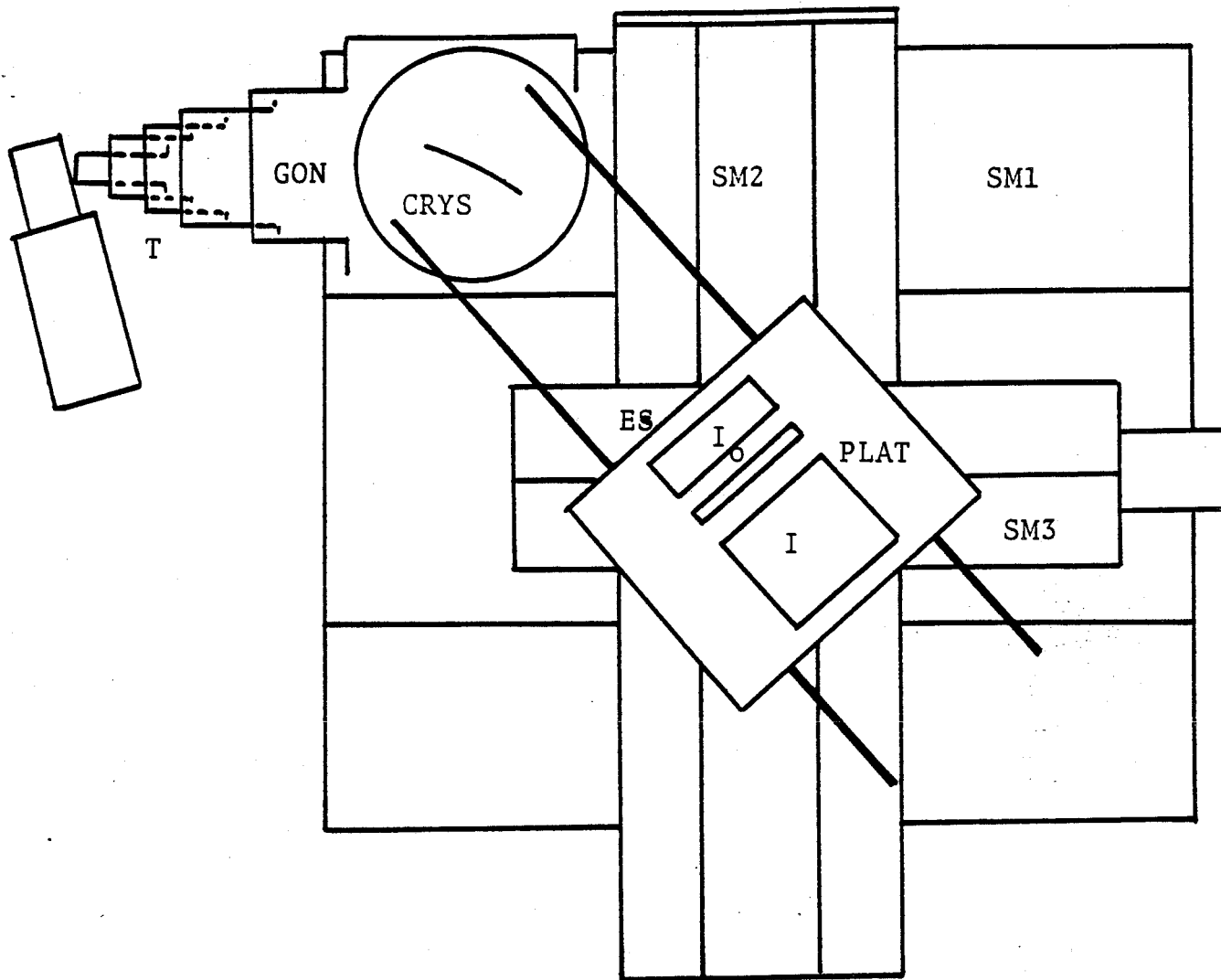
Fig. 2.9: *The spectrometer (top view), showing CRYS the crystal,
GON single axis goniometer, SM1 lower stage sliding carriage, SM2
intermediate sliding carriage, SM3 upper sliding carriage, PLAT
platform, T telescopic cylinders, ES exit slit, I_o and I
ionization chambers.*

The bent crystal is mounted on a crystal holder which is attached to the goniometer. The goniometer is driven by a stepping motor (Ealing 018) which has minimum angle increment 0.001 degree. The crystal holder has two micrometers to adjust small horizontal displacement and tilt of the crystal. The accuracy of the stepping motor was checked by using an interference method; *i.e.*, a front surface mirror was attached beside the goniometer; the interference pattern of a laser beam split by a parallel transparent glass was observed and measured on a microscope.

The translation stages consist of three UniSlide motor-driven assemblies. SM1, SM2 and SM3 are driven by Superior Electric stepping motors SLO-SYN M093-FD11, M092-FD08 and M093-FD11 respectively. A motor providing 200 steps per revolution with a double start 20 thd/inch screw thread (0.100" advance per turn) produces 0.635 mm increments per turn (3.175 microns per step). The motors are interfaced by translator modules with the computer (PDP 11/34). The total travel lengths for $x_2(x_c)$, x_1 and y_1 movements are 450, 370 and 635 mm respectively. The actual travel lengths of the stages are monitored by the Mitutoyo linear scales with an accuracy of 0.001 mm over the total length. SM1, SM2 and SM3 are monitored by Mitutoyo FN-450, FN-700 and FN-400 respectively. Several stops (LED interrupt) are mounted at the end of each translation stage to restrict movement of the stages. The detector platform is mounted on a ball bearing which is fastened

to SM3 (the upper level of the translation stage). The detector platform is aligned to the reflected beam direction by two rigid rods (each 91 cm long and with diameters 0.95 cm) which are fastened to the freely rotating part of a ball bearing on the goniometer, and which slide through linear ball bearings below the detector platform. A set of telescopic cylinders (T) made of brass (thickness 0.3175 cm) is mounted between the head of the x-ray source and the crystal to protect users from x-ray radiation.

Based on the McMaster [1969] tables, the thickness of the brass cuts down the x-ray intensity by a factor of 2.67×10^{12} for x-ray energy of 30 keV. However, the apparatus normally operates below 30 keV, meaning that the shielding reduces intensity even more. The maximum permissible dose rate is 0.1 rem/week[1] [Morgan, 1963] which is equivalent to 1.18×10^4 photons/sec/cm^2 (setting the x-ray generator at 30 kVolts). An x-ray generator with tube energy 1.2 kWatts (30 kVolts, 40 mA) at 1 meter distance produces less than 1×10^9 photons/sec/cm^2 (1 keV bandwidth at 30 keV). This radiation is certainly reduced to the safe level by the shielding.

---

[1] Roentgen Equivalent Man (rem): That amount of ionizing radiation of any type which produces the same damage to man as 1 roentgen of about 200 kV x-ray radiation.

Roentgen (R): That quantity of x-ray or gamma radiation such that the associated corpuscular emission per 0.001293 gram of dry air (equals 1 cc at 0°C and 760 mm Hg) produces, in air, ions carrying 1 esu of quantity of electricity of either sign.

1 roentgen $\approx \dfrac{2.15 \times 10^9}{E}$ photon/cm^2, E in MeV.

2.4. Detectors

In EXAFS experiments, one detector is needed to monitor the incoming beam (I_0 detector), and another is needed to measure the transmitted or fluorescent x-rays.

The ideal detector for laboratory EXAFS facilities, as described by Stern [1980], should have the following characteristics: highly linear, has a high and variable efficiency over the x-ray energy range of 2.5-20 KeV, can handle intensities up to 10^7 photons per second and has good energy resolution. For fluorescent use the detector should have a large area to maximize the counting rate.

The standard x-ray detectors are photographic films, gas ionization detectors, and solid state detectors [Clark, 1955; Jaundrell-Thompson and Ashworth, 1970; Agarwal, 1979; Hayes and Boyce, 1982]. Film is seldom used to record EXAFS scans. Two types of gas ionization detectors are commonly used in EXAFS experiments: the ionization chamber and the proportional counter. Both consist of an inert gas between two electrodes. Electron-ion pairs are produced when an x-ray photon is absorbed. In argon, for example, it takes approximately 30 eV to produce an electron-ion pair [Hayes and Boyce, 1982]. Approximately 300 electron-ion pairs are produced for each 9-KeV photon absorbed. For a given x-ray intensity the output current from an ionization detector rises

initially as the voltage across the electrodes increases and then reaches a constant value, the plateau region as indicated in Fig. 2.10, where the gain is unity and independent of the applied electric field. In this case, the detector is referred to as an ionization chamber. If the electric field in the gas is increased to about 25000 Volts/cm [Clark, 1955; Agarwal, 1979; Hayes and Boyce, 1982], the electrons produced by the x-rays are accelerated sufficiently to produce secondary electrons. This gives the detector a gain which is proportional to the applied field, up to the potential where an electron avalanche or discharge occurs in the gas. The detector operated in this mode is referred to as a proportional counter [Wilkinson, 1950].

Two types of solid-state detectors are commonly used: scintillation counters and semiconductor detectors. In a scintillation detector, pulses of visible light are produced by fluorescence resulting from the absorption of x-rays in scintillating material. The visible radiation is detected with a photomultiplier. These detectors have high gain, reasonable dead times, and relatively poor energy resolution. For standard NaI(Tl) scintillation detectors, for example, the dead time and energy resolution are on the order of 1 microsec and 4000 eV at a 10-keV photon energy. Semiconductor detectors are Si or Ge crystal compensated with Li. They have an intrinsic gain of unity but short dead time (about 10 ns) and good energy resolution (about 200 eV) at a 10-keV photon energy [Hayes and Boyce, 1982].

27
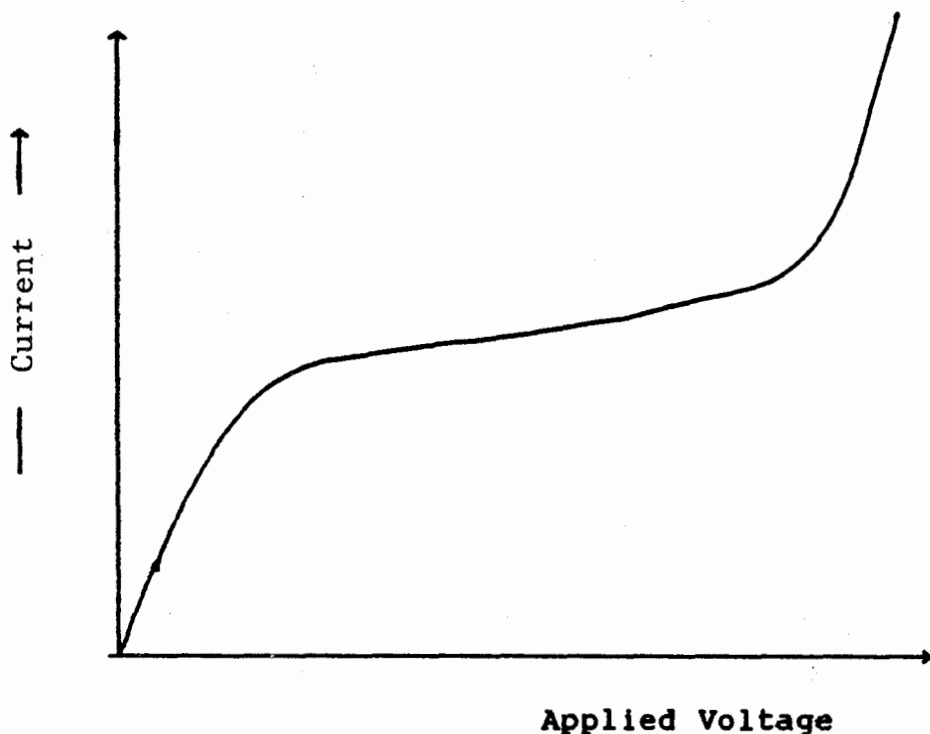
Fig. 2.10: *I-V characteristic. Effect of voltage on resulting current rate for constant x-ray intensity.*

In our laboratory, we use home-made ionization chambers made of brass rectangular boxes with kapton windows (to reduce noise, kapton can be changed to thin aluminum mylar). Their planar aluminum electrodes have a spacing of 14 mm and lengths of 30 mm (I_o) and 120 mm (I). The ionization chambers are operated at about 130 Volts DC. The chambers are filled with argon gas flowing continuously.

2.5. Alignment

2.5.1. Determine the center of the rotation stage

a. Align Aluminium Base Center Line

An Al base (see Fig. 2.11) is placed on the top plate of the rotary stage (GON in Fig. 2.9). Bolts are inserted but are not tightened yet. A dial gauge is used to adjust the Al base centerline to be collinear with the rotation axis. Bolts are tightened and never loosened again.

b. Centering the Base Plate of the Crystal Holder

The base plate (see Fig. 2.11) is positioned on the Al base. Four bolts are used to locate the base plate. These bolts are tightened and never loosened again.

c. Moving the Center of Rotation

Once the center of rotation is known, another device (see Fig. 2.11) is used to extend the center to the level of the crystal position. This device consists of a flat plate placed parallel to both base plates, plus a vertical plate and a pointer. A mark is drawn through the center of rotation on the horizontal plate. The mark is continued to a pointer mounted on the vertical plate by

using a surface plate available in the Science Workshop. This procedure determines the position of the pointer in the center of rotation with an accuracy of about 0.005". The pointer is extended vertically with a needle supported by a holder (see Fig. 2.12). This needle, which we call the θ needle, is then used in aligning the exit slit.
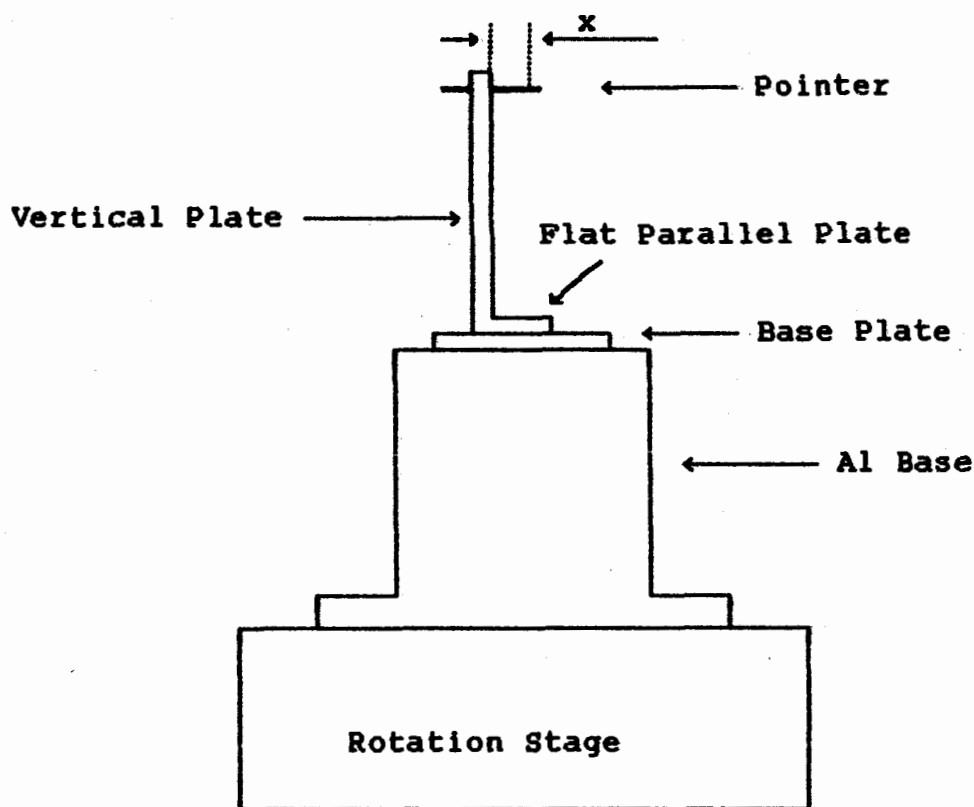
Fig. 2.11: *Centering the rotation stage to define the axis of rotation of the crystal.* x *is 1.89 cm.*
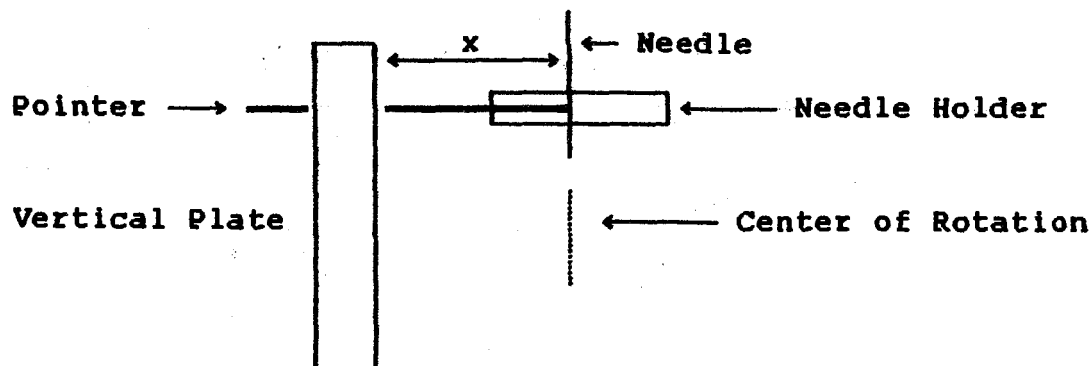
Fig. 2.12: *Center of rotation position. The diameter of the needle is 0.071 cm. x is 1.855 cm.*

2.5.2. Align the position of exit slit

Before the exit slit was mounted, the width of the slit was calculated from a one-slit diffraction experiment using a He-Ne laser ($\lambda = 6.326 \times 10^{-7}$ cm), see Fig. 2.13. The calculated width is 244 ± 7 μm. The slit is then mounted on a movable housing. The horizontal position of the slit can be adjusted by a micrometer.
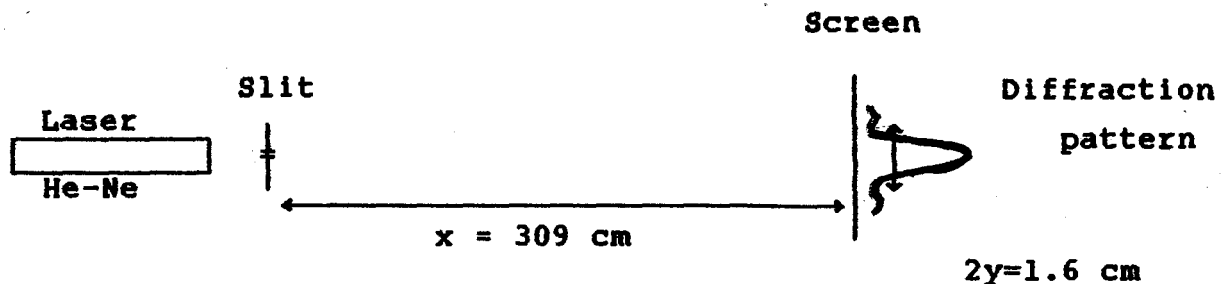
Fig. 2.13: *One-slit diffraction experiment to determine the exit slit.*

As follow-up to section 2.5.1, another needle is placed in the center of rotation axis of the sample position (PLAT in Fig. 2.9). The needle is held by a copper cylinder and is aligned to the centre of the rotation by using a dial gauge. In subsequent steps, an x-ray source, I_o and I chambers are used (see Fig. 2.14).

The purpose of the alignment is to place the exit slit on a line between the θ and sample needles. The x-ray source is turned on and the currents from I_o and I chambers are recorded. The y axis (y_s) is moved perpendicular to the x-ray beam and the I_o and I readings are recorded with a two-pen strip chart recorder. As y is scanned, I_o will have a single minimum due to the shadow of the θ needle and I will have 3 minima, one due to the θ needle and two due to the sample needle.

If the exit slit is at the correct position (on the line between the two needles), then the position of the minimum recorded by the I_o chamber will be at the same position as the central minimum recorded by the I chamber, and two other minimum positions of the I chamber will be at symmetrical positions (at equal distances from the central minimum). If the exit slit is not at the right position, then the I_o minimum and the central minimum of the I chamber will be at different positions upon moving y_s. From the asymmetrical position of the other minima of the I chamber, it can be determined which way the exit slit must be moved horizontally

32

to the correct position. The process is repeated several times.
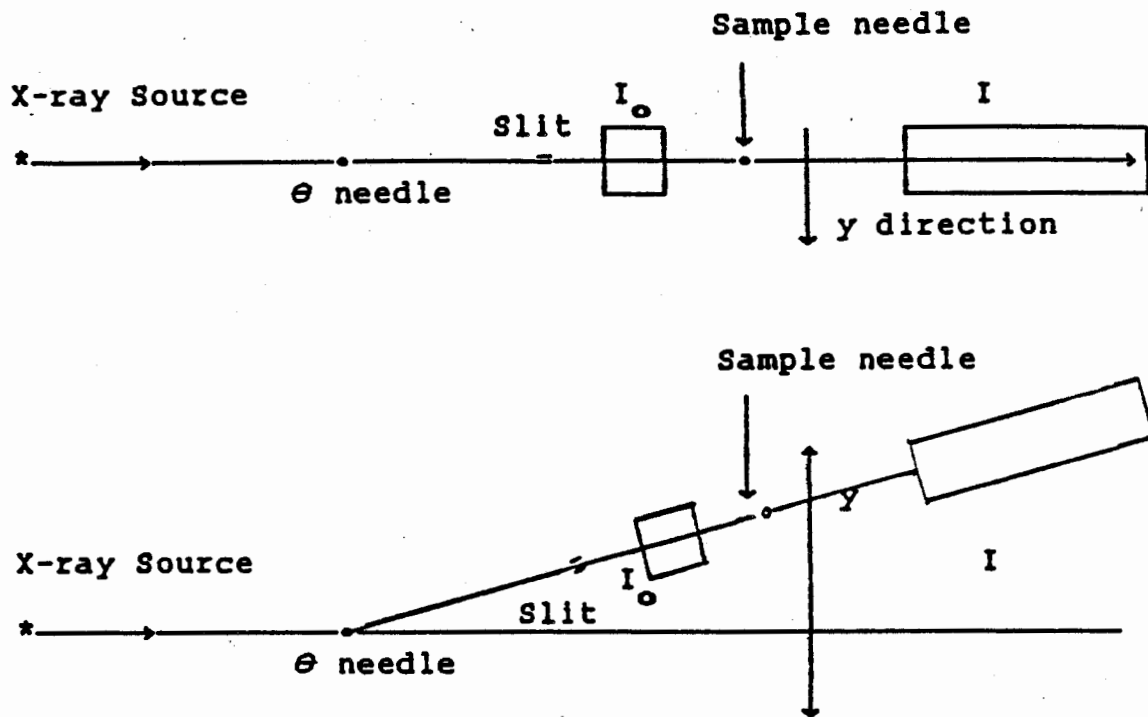
Fig. 2.14: *Exit slit positioning. The upper diagram shows the source, the θ needle, the exit slit and the sample needle on line. In the initial setup, the exit position is unknown, and the y position is moved to determine the correct position of the exit slit (lower diagram).*

After finding $y_s = 0$ as described in the next section, another test is performed by removing the θ needle. The horizontal position of the exit slit is deliberately moved away from the correct position by a certain distance. The y_s axis is then moved,

and the minimum and maximum positions of the I chamber after this movement are recorded. Subsequently, the exit slit position is moved in the opposite direction by the same distance, and a similar recording is performed. The minima must be symmetrically positioned with respect to the zero position reference of y. The position of this slit on the micrometer scale is 0.537 cm.

2.5.3. Defining the Zero Position of the y-axis

A slit of width 1 mm was first inserted on the x-ray housing of the x-ray tube. The slit was centered by adjusting its position until maximum intensity was recorded by an ionization chamber placed 3 cm from the housing.

A needle placed in the center of the rotation stage (θ needle) is used to determine the zero position of the y-axis. The x-ray source is turned on and the "shadow" of the needle on the exit slit is recorded by moving y_s. The procedure is repeated for several different positions of x_c.

From this measurement, the position of the head of the x-ray source can be adjusted until the shadow of the needle remains at the same position on y_s while the translation stage x_c is moving. The position in this case is equivalent to $y_s = 0$ and it is electronically stored on the counter. The position relative to a mark point (absolute scale) of y_s scale is recorded. This

34

recording is necessary in the event of total power failure. The y_a position at the mark position is 10.099 mm. This mark position is the first mark of the y_a scale counting from lower y.

The diameter of the needle at the rotation stage is 0.71 mm and at the sample position is 0.63 mm. The position of the x-ray housing (on the scale to determine the relative position) is 0.589".

2.5.4. Crystal Bending apparatus

Several methods to bend a crystal to focus x-rays and discussions of its characteristics have been mentioned by several authors [DuMond *et al.*, 1947; White, 1950; Witz, 1969; Frank and Breakwell, 1974; Webb, 1976; Borchert *et al.*, 1980; Crane, 1980].

The bending scheme used in our laboratory is similar to that described by Crane. The bender consists of four cylindrical rods (length 7.5 cm, diameter 0.32 cm) held by two separate brass plates (see Fig. 2.15). The crystal (length 6.5 cm, width 3 cm and thickness 400 μm) is placed between the plates, and the rods give a bending moment at both ends of the crystal. The plates are held by ten bolts to adjust the bending radius. The crystal bender is then attached to an adjustable mirror mount which has two micrometers to adjust the position of the crystal vertically and horizontally.
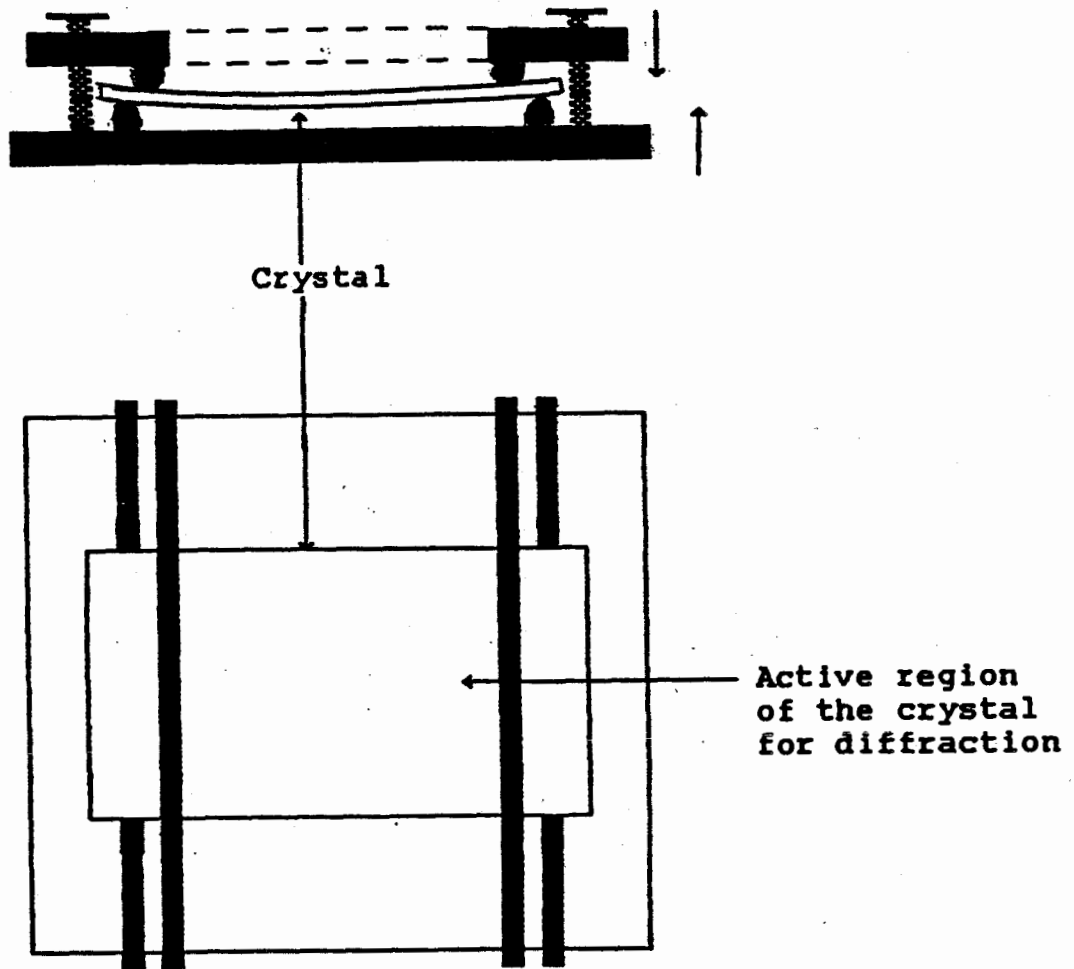
Fig. 2.15: *Crystal bending apparatus. The upper drawing shows the bend as viewed from the top. The lower drawing is a side view, showing one of the brass plates, four cylindrical rods, and the crystal which is held between these rods.*

By using this bending scheme, a cylindrical curvature can be obtained. The scheme has further advantages: the bending can be varied by adjusting the bolts, and dust between the crystal and the backing plate used in other designs is not a problem. However, there are some drawbacks to this scheme: it is not possible to achieve perfect cylindrical symmetry; it is not known how large a crystal may be bent successfully in this way; and one is never sure exactly what shape the crystal has taken.

The geometry can be checked and corrected using an "eye-balling" method [Templeton, 1986], i.e. after the crystal is mounted and bent, a sharp tiny object is placed in front of the bent crystal and the image in the crystal is observed by the eyes. Any irregularity of the image tells that the crystal has not been bent properly. The ten bolts are used to adjust the crystal until a proper image is seen. This "eye-balling" method also gives a rough estimate of the radius of the crystal.

The crystal is further checked by an optical scheme, i.e. a laser beam is passed through a narrow line slit, and the image of the reflected beam is observed on a screen. If the crystal is bent cylindrically, the image forms a line. The laser beam is also used to determine the radius of curvature of the crystal by assuming that the bent crystal is a converging mirror. From the experiment, the focal length is 354.5 ± 0.5 mm. For a Johann-type crystal, the focal length is the Rowland circle radius.

2.5.5. Adjusting Crystal Position
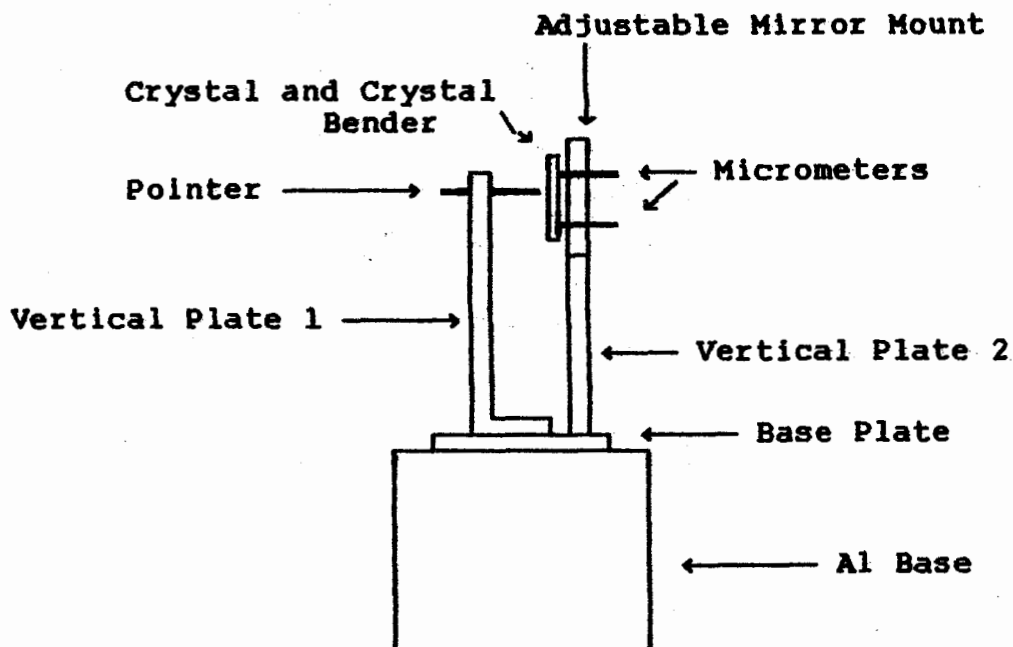
Fig. 2.16: *Crystal position alignment.*

The θ needle (from alignment in section 2.5.3) is removed. The crystal bender is placed on the top of vertical plate 2 of the crystal holder (see Fig. 2.16). The two micrometers are adjusted such that the crystal touches the pointer (center of rotation).

After the crystal is mounted, the x-ray beam is observed (recorded) by using a Polaroid film placed approximately at the focal point of the monochromator to check whether the crystal has
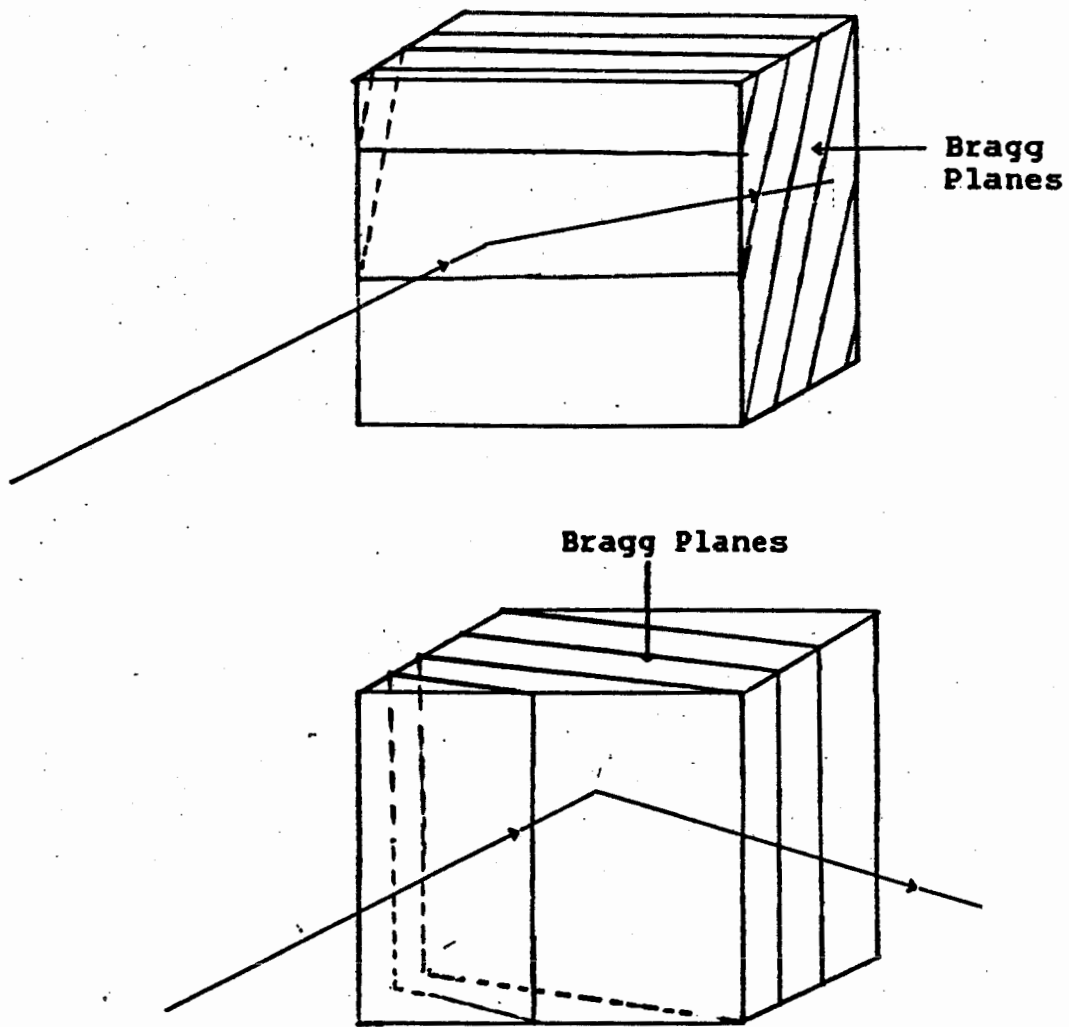
Fig. 2.16: *Crystal orientation. The top crystal shows that the x-ray beam is reflected in a wrong direction. The crystal is rotated 90° to get a correct orientation.*

been properly installed in the correct position. The first photographs showed that the reflected beam was not at the expected focal point. However, when the crystal position was checked by using a laser beam in reverse order (the laser beam source was placed behind the exit slit, and a screen placed on the x-ray head), the result showed that the crystal was properly aligned. This discrepancy led to the conclusion that the Bragg planes of the crystal were not parallel to the surface of the crystal.
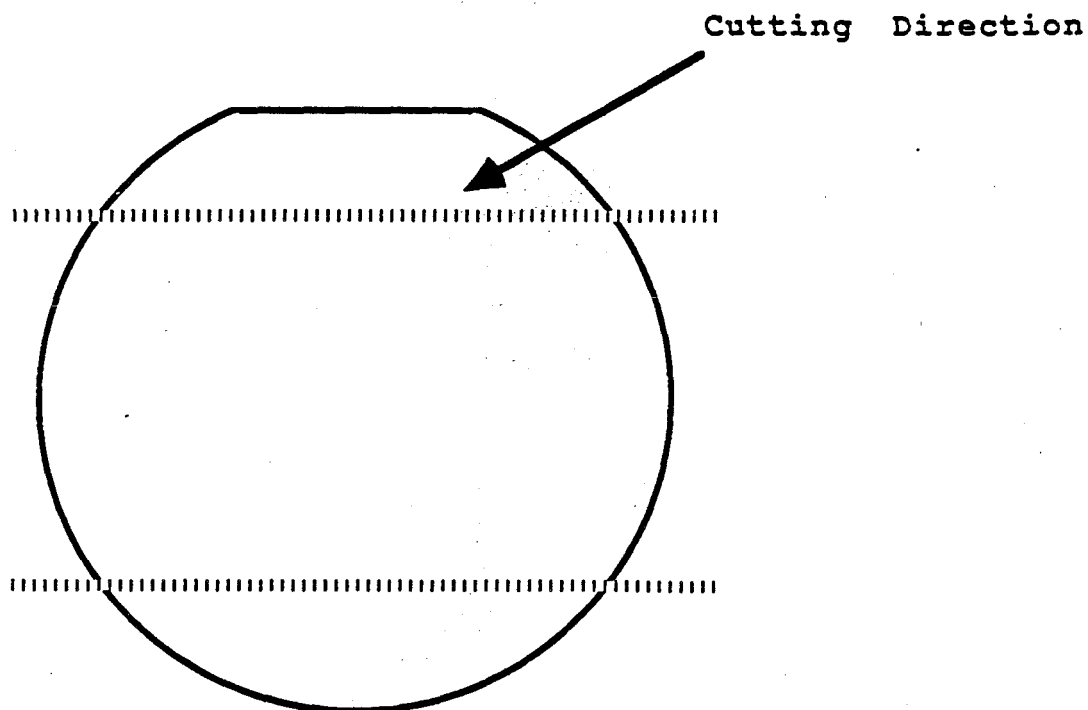
Fig. 2.18: *Orientation for cutting the crystal. The crystal is cut parallel to the flat side of the wafer.*

A Laue photograph taken to examine the crystal revealed that the orientation of the Bragg planes (111) was not parallel to the crystal surface, but tilted with respect to the surface by $3.6°$. To get a correct orientation, the crystal was rotated $90°$ (see Fig. 2.17); in other words, the crystal was cut parallel to the flat side of the crystal wafer (see Fig. 2.18).

2.5.4. Determine the Zero Position of the x-axis

At this point, y_1 is known accurately, but x_1, x_2 and θ still have be corrected by constant offsets.

$$x_1' = x_1 + x_{1off} ,$$

$$x_2' = x_2 + x_{2off} , \qquad\qquad (2.7)$$

$$\theta' = \theta + \theta_{off} ,$$

where primes denote the measured values.

The following procedure is used to determine the first estimate of the offsets: The exit slit defining x_s and y_s is placed at a certain position. The x_c (or x_2) is changed until the recorder in the I_o chamber shows maximum current, and the four parameters are recorded.

Upon finding maxima in I_o by moving x_a, the other three stages (y_a, x_1 and θ) are moved one by one until an absolute maximum is found. The parameters are then varied to a different position and a similar experiment to find the position of absolute maximum intensity is performed again. By comparing one position with another and by using equations (2.2), (2.5), (2.6) and (2.7), the positions of x_a, x_2 and θ are calibrated.

$$x_2 = 2 R \sin (2 \theta - 2 \theta_{off})$$

$$y_a = (x_2 + L) \sin (2 \theta - 2 \theta_{off}) \qquad (2.8)$$

$$x_a = (x_2 + L) \cos (2 \theta - 2 \theta_{off}),$$

From the equations, one can derive:

$$y_a/x_a = \tan (2 \theta - 2 \theta_{off}), \qquad (2.9)$$

θ and x_a are calibrated, and then, the result is used to calibrate x_2.

The absolute calibration is done by searching for emission lines of the tungsten target of the x-ray tube. Initially, from the energy where the emission line is, the four parameters (x_a, y_a, x_2 and θ) are calculated, and then by using the calibration results described in the previous paragraphs, all the motors are moved to

their respective positions. Subsequently, all four parameters are varied (by moving the motors) until an absolute maximum reading in I_o is found. The results are tabulated in Table 2.1: for each emission line, the first row gives the initial calculated values and the second row gives the measured values.

Table 2.1: Emission Lines

Emission Lines	E (keV)	θ	x_1	y_1	x_2	i (A)
$L\beta_1$	9.671	37.831	129.242	505.614	433.625	
		37.819	129.621	505.957	461.118	0.112×10^{-9}
$L\beta_2$	9.960	36.551	148.039	487.298	421.043	
		36.537	148.510	487.973	439.029	0.492×10^{-10}
$L\gamma_1$	11.284	31.713	205.738	411.299	371.64	
		31.696	206.485	411.923	387.481	0.308×10^{-10}

The measured and calculated values are compared to calibrate θ, x_1 and x_2. The calibration results are stored electronically on the counters. The reference point of x_1 is at −22.554 mm measured from the lower position of x_1. The reference point of x_2 is at 500.544 mm measured from the high position of x_2. The θ scale is calibrated within 1.76 millidegrees, this error giving uncertainty in the absolute energy of about 0.528 eV for Si(333) at 11 keV. Table 2.2 shows the errors for several energies.

Table 2.2: Energy Error Due to Uncertainty in θ

Energy (keV)	Crystal	Error
4	Si(111)	0.216
8	Si(111)	0.962
8	Si(333)	0.222
11	Si(333)	0.528
18	Si(333)	1.584

Summary of the alignment results:

1. The exit slit position on the micrometer scale is 0.537 mm

2. The x-ray head position on the scale is 0.589"

3. The Rowland circle radius (Johann-type) is 354.5 ± 0.5 mm

4. The reference points of the translation stages are in Table 2.3

Table 2.3 : Reference Points

Translation Stage	Reference Point	Measured from	Switch Direction
x_1 (1)	-22.554 mm	lower scale	left
x_2 (2)	500.544 mm	higher scale	right
y_3 (3)	10.099 mm	lower scale	left

Chapter 3

AUTOMATIC SYSTEM

As indicated in the beginning of the previous chapter, an EXAFS laboratory facility is used to measure the x-ray absorption coefficient of a sample at a given x-ray energy, change this energy by some predetermined amount, then re-measure the absorption. The cycle is repeated for many different energies and the data are stored in some form for later analysis. Each measurement produces large amounts of data; hence, for efficiency, some means of automation is needed. Automating an EXAFS facility has been discussed by several authors [Elam, 1980; Georgopoulos *et al.*, 1980]. The basic steps in our laboratory routine (see Fig. 3.1) are: set the Bragg angle of the crystal for a certain energy, move the translation stages to place the exit slit in the Rowland circle, measure the signals of the incident and transmitted x-rays, pass the signals to a DC-to-frequency converter and integrate for a preset time, and finally record the counts along with the Bragg angle on a disk. This process is repeated for different energies.

The computer (PDP 11/34 with RT-11 operating system) through a CAMAC interface is used to control the whole movement of the

spectrometer, record the data and do some preliminary analysis to assess the quality of the data, detecting the possible presence of unwanted effects in an EXAFS experiment (harmonic contamination, pinholes in the sample [Stern and Kim, 1981; Goulon *et al.*, 1982], crystal glitches [Bauchspiess and Crozier, 1984], *etc.*).
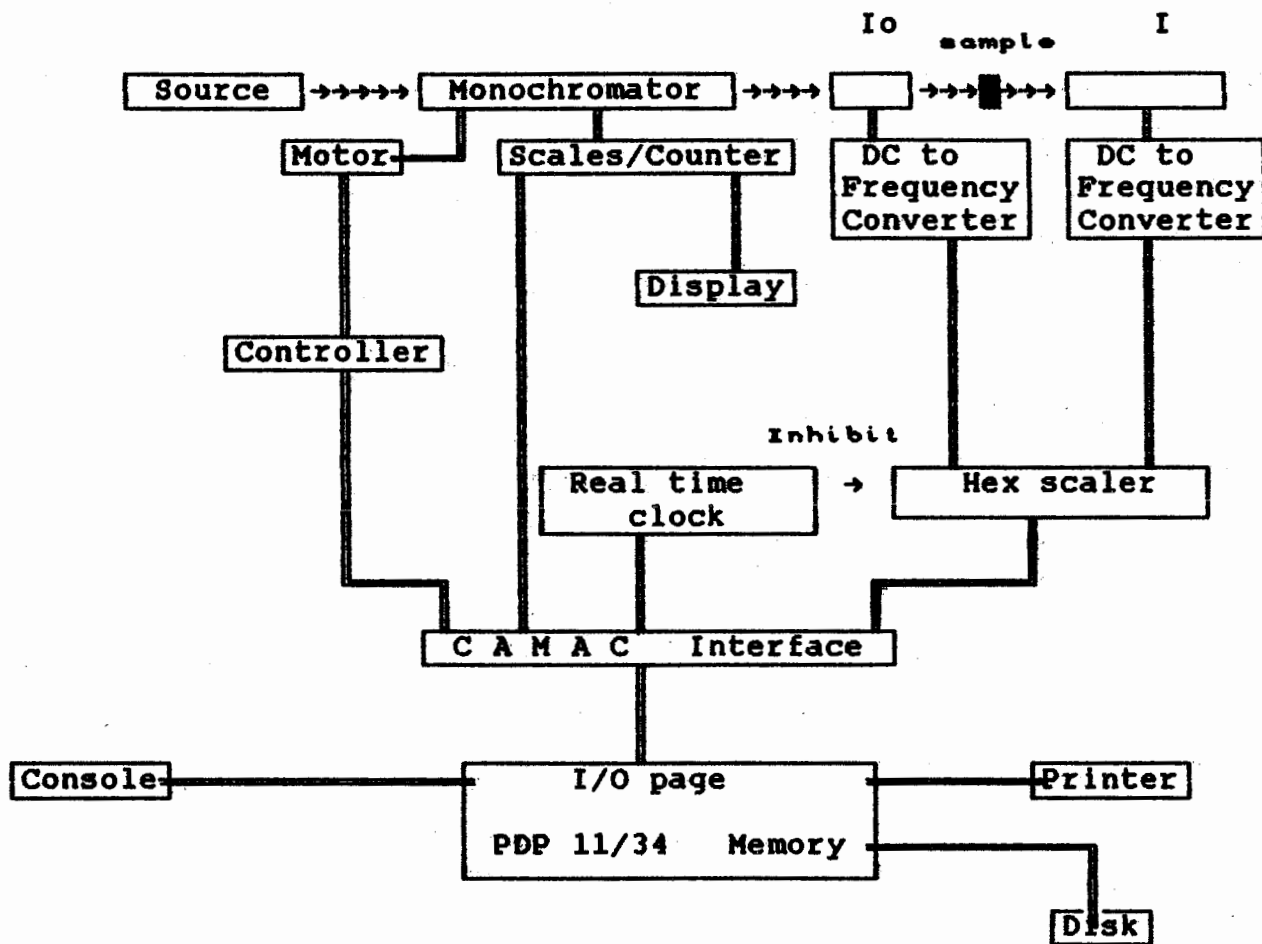
Fig. 3.1: *Block diagram for laboratory EXAFS apparatus.*

The x-ray energy is changed by a stepping motor under computer control. An intermediate controller is used to adjust the logic signal from the computer to switch the high current required by the motors (theta and three translation stages). After the spectrometer is set at a certain energy, the ionization chambers measure the x-ray flux. The signals are amplified and then sent to DC-to-frequency converters (Anadex model 1700-5044-00), whose output is a series of pulses whose frequency is proportional to the input signal. The pulses are counted by a scaler (3610 Hex Scaler from KineticSystems Corporation). A timer (Real Time Clock RTC-018 from Standard Engineering Corporation) inhibits the process after a certain period of integration time. The scaler and the timer are controlled by the CAMAC interface which takes all commands from the computer. The data are stored in the disk of the computer.

3.1. Hardware

The basic computer hardware in the laboratory consists of the central computer, program and data storage, and the interface to the electronics. In addition to these, it is also necessary to have a graphics terminal and some means of transferring data from the central computer to other systems.

The central computer in our laboratory is a PDP 11/34 minicomputer. The PDP-11 family is a product of DEC (Digital

Equipment Corporation). It is a 16-bit minicomputer (it has direct addressing of 32 K 16-bit words) with the following characteristics: asynchronous operation, modular component design, direct memory access, automatic priority interrupt (four-line system permits grouping of interrupt lines according to response requirement), vectored interrupts (fast interrupt response without device polling) and power fail & automatic restart. The central processor, connected to a UNIBUS as a subsystem, controls the time allocation of the UNIBUS for peripherals and performs arithmetic and logic operations and instruction decoding. It contains multiple high-speed general-purpose registers which can be used as accumulators, address pointers, index registers, and other specialized functions. The processor can perform data transfer directly between input/output devices and memory without disturbing the processor registers. The operating system used is RT-11, a small, single-user foreground/background system that can support a real-time application job's execution in the foreground and an interactive or batch program development in the background.

Dual disk drives are used, in which the spectrometer driver programs are stored on one diskette and data on the other. An additional storage device (hard disk) is used to store other programs and data.

A CAMAC is used to interface the computer and all other electronics equipment in the laboratory (scaler, timer, motor

controller, and scales/counter for the translation stages and theta). This multiple-crate CAMAC (type 1533B) is linked to the UNIBUS as the means of interconnection between the PDP-11 and the various crate controllers. During each UNIBUS cycle the computer can communicate with any of up to ten crate controllers. An addressed on-line crate controller accepts a command via the UNIBUS and generates the corresponding crate dataway command containing station number, sub-address and function.

The model 3610 hex scaler (6-channel, 50 MHz counter) is a single-width CAMAC module containing six 24-bit counters. These counters accept input and can count frequency up to 50 MHz. The counters can be inhibited by dataway inhibition or by a front-panel signal. All the six counters can be used at the same time, allowing simultaneous experiments.

The model RTC-018 real-time clock is used in timing and controlling the experiments. This timer is loaded with values determined by the experimental setup file, and counts down to zero. On reaching zero, it sends an inhibit signal to the front panel of the hex scaler.

The type 1700-5044-00 DC to frequency converter provides an output frequency that is directly proportional to the DC input signal. The output frequency range is nominally from 0 to 1 MHz with input of 0 to 10 volts. The conversion factor of the three ports of this

equipment is 100 kHz/volt. At the moment, only two ports are used; one each to receive the I_o (incident beam) signal and the I (transmitted beam) signal. In later development, the third port can be used for other purposes, such as fluorescence experiments.

The motor controller (made by the SFU electronics shop) converts logic signals from the computer to the high current signals required by the motors. The controller also reads the four position counters and checks the limit switches, placing their values on the CAMAC dataway where they are available for the computer [Seary, 1987].

3.2. Software

The setup experimental programs were written in FORTRAN, by Andrew Seary, and then translated into the computer's machine language by a compiler with RT-11 operating system for the PDP 11/34. The driver programs were for the most part written in FORTRAN, but for efficiency, some parts were written in assembly language (for hardware driver and timing routines). The program package was written such that from the user's point of view, it has similar features (regardless of hardware configuration) to the program written for EXAFS experiments at SSRL (Stanford Synchrotron Radiation Laboratory).

The data analysis programs were written in APL for the university

mainframe (IBM 3081 GX running the MTS operating system) by using VS APL, or alternatively using STSC APL for an IBM PC machine or compatible; we can also analyse data on the 11/34 using DEC APL. This data analysis package is the same on the three systems, except for hardware-dependent features such as graphics. The same package is used for analyzing SSRL data.

The functions of the programs for running the EXAFS apparatus can be divided into several major areas: [Elam, 1980]

- initialization and hardware setup, such as monochromator calibration
- software setup, such as selecting the scan range
- data acquisition
- data analysis

3.2.1. Initialization and hardware setup

Before anything else is done, the program must first read the initial position of the monochromator, as given by the position of theta and the position of the three translation stages. The counter for the theta position is set to some initial known position value and the positions of the translation stages are recorded by the linear scales. These scales show the absolute position of the stages.

The program must also include hardware initialization, *i.e.*

51

specification of several constants required by the program to
describe the hardware configuration during the running of the
experiment. Other constants are also required for conversion of
the theta position to energy, including the lattice spacing of the
monochromator crystal.

This information is stored in a master file, from which many
different files for different setups of experiments can be
produced. The master file also holds the information of hardware
parameters which are seldom changed, such as the bending radius
and lattice spacing of the crystal, and several time-dependent
parameters which change fairly frequently.

3.2.2. Software Setup

Selecting the scan range is necessary before data are taken.
Furthermore, different setups can be used for x-ray energy scan
(E-scan) or photoelectron momentum scan (k-scan). All parameters
must be specified in advance and saved in a setup file. The
parameters associated with scanning are the starting and ending
points, the increment size, and the integration time. These scan
parameters are specified directly in energy in eV or photoelectron
momentum in $\mathring{A}^{-1}$ It is useful to have these parameters since the
program is capable of selecting different regions with different
step sizes, reducing the time spent in taking data. Only a few
points are taken below the edge, more points are taken around and

above the edge, and a fairly coarse increment can be taken far above the absorption edge.

3.2.3. Data Acquisition

The process of data acquisition consists of the following steps: move the monochromator position (theta), move the three translation stages, read all motor positions, read the incident flux (I_o), read the flux transmitted through the sample (I), write theta, I_o and I to a file, change theta, move the translation stages, and repeat the procedure.

There are also a few other details of taking and storing data, such as keeping up with the increment in theta, the starting and the ending values, the name of the file in which data is stored and some comment about the scan (the name and condition of sample, the source, *etc.*).

Several extra features are added to save time and energy, such as a simple check to see that the x-ray beam is on by ensuring I_o is above some preset minimum, and a check that the translation stages are still on the operational range (do not hit the stops). The program also has the ability to do multiple scans, and can handle up to 6 scalers, allowing for simultaneous transmission and fluorescence experiments, or collecting data on a reference sample of known structure [Seary, 1987].

3.2.4. Data Analysis

As indicated earlier, preliminary data analysis is included in the package to get a rough estimate of the quality of the data. The analysis includes: plotting the raw data (I_o or I vs. theta), log I_o/I vs. energy, plotting on a graphics terminal elementary analysis of the EXAFS oscillation in k-space and in R-space the Fourier transform (real part, imaginary part or magnitude) of the k^n weighted EXAFS interference function $\chi(k)k^n$. Subsequently, the data is transferred to a different system for further analysis.

On the other systems (University mainframe/MTS, IBM PC compatible, or DEC APL) the data are analyzed in a similar fashion as the data from SSRL. A comprehensive EXAFS software package has been developed for data analysis for these systems.

At first the program reads the raw data (set data of theta position, I_o and I) and converts it to the logarithm of I_o/I vs. energy. The result is displayed on the screen (CRT) by using a graphics routine in APL. By using a Victoreen fit [Lytle et al., 1975] absorption background is removed. The inflection point (k=0) is determined by picking the maximum point of the derivative of the absorption vs. energy around the edge. After finding the inflection point (a point, which at least in a pure metal, is taken to be the threshold for absorption [Hayes et al., 1976]), a

grid calculation is used to convert the energy scale to the momentum scale (k). After this conversion, the EXAFS oscillation in k-space is displayed on the CRT. The data are then normalized under certain weighted values of k. A Fourier transform is then applied to permit examination in real space.

All the steps mentioned above use the interactive mode in APL. The graphics displays are very useful in picking up several points or ranges in the analysis. Further analysis with examples is discussed in chapter 5.

Chapter 4

Performance

4.1. Data Collection

4.1.1. Intensity

The intensity of the Bremsstrahlung, integrated over the whole spectrum, is given by [Fisher, 1980]

$$I_{tot} = k \; i \; Z \; V^2 \qquad\qquad (4.1)$$

where k is a constant $(1.5\pm0.3)\times10^{-9}$ related to the Bremsstrahlung cross-section, i is the tube current, Z is the atomic number of the target, and V is the accelerating voltage of the tube.

In our lab, an x-ray generator is used with a water-cooled sealed tube with a tungsten target. The accelerating voltage can be increased up to 50 kVolt and the current up to 45 mA, but the accelerating voltage must be kept below the excitation level of higher harmonics which might be diffracted by the monochromator crystal. The take-off angle of the x-rays was set to 8° by the telescope used for radiation shielding.

56

The photon flux N_o at the exit slit (width 240 μm) can be evaluated from the measured ionization current I_o according to

$$N_o = I_o E_i / e E [1 - exp(- \mu d)], \qquad (4.2)$$

where E_i is the average ionization energy per ion-pair in the ionization chamber with length d and absorption coefficient μ. Operating the x-ray generator at 15 kVolt and 31 mA with a tungsten anode, and ionization chamber with d = 30 mm filled with argon gas at atmospheric pressure, an ionization current of I_o = 0.051×10^{-11} A was measured at a photon energy of E = 11000 eV. With average ionization energy of E_i = 30 eV, and μ argon of 0.0987 cm^{-1} at 11 keV (from McMaster tables), a photon flux of N_o = 3.39×10^4 photons/s can be calculated from equation (4.2). When the generator is operated at 20 kVolt and 40 mA, a photon flux on the order of 10^5 photons/s can be obtained.

4.1.2. Linearity of Detection System

The detection system for the experiment has been tested. The tests involved: examining the characteristic of the ionization chambers for difference voltages, checking the linearity of the picoammeter (Ithaco Model 1211 amplifier), and calibrating the DC-to-frequency converter and the computer system.

The I-V characteristics of the I and I_o chambers were examined by feeding several different voltages from 0 to 600 volts to the chambers. The x-ray was turned on (at voltage 20 kV and current 40 mA) and directed to the chamber (θ was set 31.193°, x_1 = 211.085, x_2 = 367.180 and y_1 = 403.554), and the currents measured. The results show that the I_o chamber reaches the plateau region (see Fig. 2.10) at voltage 11 volts, and I chamber at about 3 volts. Both chambers are still in the plateau region above 600 volts.

The linearity of the picoammeter was checked by feeding currents from a picoampere source (261 picoampere source from Keithley Instrument Inc.) and the voltages were measured. The output and the input of the apparatus have a correlation factor of .9999976 (highly linear).

The DC-to-frequency converter was calibrated separately. Input voltages over the range 0 to 10 volts DC , measured by a voltmeter (Fluke 8810A), were fed in to the input of the converter. The output showed square wave voltage. The frequency was recorded by a frequency meter (5327A Timer Counter, Hewlett Packard). The zero control of the converter was adjusted such that a zero input gives zero output, and the span control was adjusted such that an input voltage of 10 volts gives 1 MHz output frequency.

The calibration was done to the three ports of the converter. All the ports showed linear correlation between the input and output.

The conversion factors (from the top ports to the bottom) are 100.00224, 100.00529 and 99.8712 kHz/volt, respectively. The correlation factor between the voltage input and the frequency recorded is 1 for the three ports.

The linear response of the computer system was checked by feeding DC signals to the DC-to-frequency converter and recording the output data on the computer. This measurement showed that the computer has a linear response (the correlation factor being practically 1).

4.1.3. Signal-to-Noise

There are many sources of signals which can modify or add structure to an absorption spectrum, thereby reducing the information which can be extracted from the measured EXAFS spectrum. These can be classified into two sources [Hayes and Boyce, 1982]: statistical noise (all fluctuations of a statistical nature, such as the intrinsic measurement error in detecting a finite number of photons and the noise figure of the amplifiers) and systematic distortions (x-ray source instabilities and variations, harmonic contamination of the beam, detector nonlinearities, and sample inhomogeneity).

The noise level of the picoammeter is about 10^{-14} A. The statistical noise is given by $N_o^{1/2} = 100$ photons/s which is

equivalent to a noise current of 2×10^{-14} A. It has been observed in our laboratory that the most dominant noise comes from the ionization chambers, about 1×10^{-13} A. The x-ray source has 0.1% kV stability and 0.02% mA stability. The harmonic contamination can be removed by reducing the accelerating voltage of the x-ray generator. Great care must be taken to prepare the sample.

An optimum signal can be calculated in the following way [Kincaid, 1975]: suppose that N_1 photons/sec are absorbed in ionization chamber 1 (I_o chamber) and N_2 are transmitted through the sample and are stopped in the I chamber per second:

$$N_1 = N_o (1 - e^{-\mu_1 x_1})$$

$$N_2 = N_o e^{-(\mu_1 x_1 + \mu_s x_s)}$$

(4.3)

Here N_o is the incident photon flux, μ_1 is the absorption coefficient for I_o chamber, x_1 is the length of I_o chamber, μ_s is the sample absorption coefficient, and x_s is the sample thickness. The fluctuation in N_1 and N_2 due to photon counting statistics are then $(N_1)^{1/2}$ and $(N_2)^{1/2}$ respectively. Except for a constant of proportionality depending on the gains of the ionization chambers, the ratio, R, of the current in the I chamber to that in the I_o chamber is

$$R = \frac{e^{-\mu_s x_s} e^{-\mu_1 x_1}}{1 - e^{-\mu_1 x_1}} . \tag{4.4}$$

The rms fluctuation in R due to photon statistics then becomes

$$\Delta R = R \left[\left(\frac{\Delta N_2}{N_1} \right)^2 + \left(\frac{\Delta N_2}{N_2} \right)^2 \right]^{1/2} = R \left(\frac{1}{N_1} + \frac{1}{N_2} \right)^{1/2} \tag{4.5}$$

The signal, S, to be optimized is the small variation in R with energy that characterizes EXAFS

$$S \propto \frac{dR}{dE} = R \, x_s \, \frac{d\mu_s}{dE} .$$

So the signal-to-noise ration S/N is

$$S/N = x_s \frac{d\mu_s}{dE} \left(\frac{1}{N_1} + \frac{1}{N_2} \right)^{-1/2} \tag{4.6}$$

$$= (N_o)^{1/2} x_s \frac{d\mu_s}{dE} \left(\frac{1}{1 - e^{-\mu_1 x_1}} + e^{\mu_s x_s} e^{\mu_1 x_1} \right)^{-1/2}$$

Maximizing this with respect to sample thickness x_s gives an optimum sample thickness:

61

$$\mu x = 2.55 \qquad\qquad (4.7)$$

4.1.4. Energy resolution

Due to the angular divergence of the x-ray beam emerging from the x-ray tube, a finite bandwidth passes through the monochromator to the exit slit. The monochromator energy resolution is defined as

$$\Delta E = (E \cot \theta) \, \Delta\theta_B \, , \qquad\qquad (4.8)$$

where $\Delta\theta_B$ is the full width at half maximum (FWHM) range about the mean diffraction angle θ_B. The energy resolution can be calculated by two methods: by measuring the white line of an EXAFS spectrum in the laboratory for a certain sample and comparing the broadening with that of a similar spectrum taken at SSRL with a certain convolution function, or by calculating the divergence of $\Delta\theta_B$ due to such factors as the size of the source, the crystal and the exit slit.

One can assume that the resolution function can be described by a Gaussian of the form [Lengeler and Eisenberger, 1980]:

$$g(E-E') \, dE' = (2\pi\tau^2)^{-1/2} \exp \, [-(E-E')^2/2 \, \tau^2 \,] \, dE', \qquad (4.9)$$

where τ is a parameter which characterizes the Gaussian. The FWHM

of this Gaussian is $(2\ln2)^{1/2}\tau$. Written in terms of the photoelectron momentum wavevector defined in (1.2), this becomes:

$$h(k,k')dk' = (2\pi\tau^2)^{-1/2}(\hbar^2 k'/m) \; x$$
$$\exp[-\hbar^4 k^2 (k'-k)^2/2\tau^2 m^2] \; dk' \qquad (4.10)$$
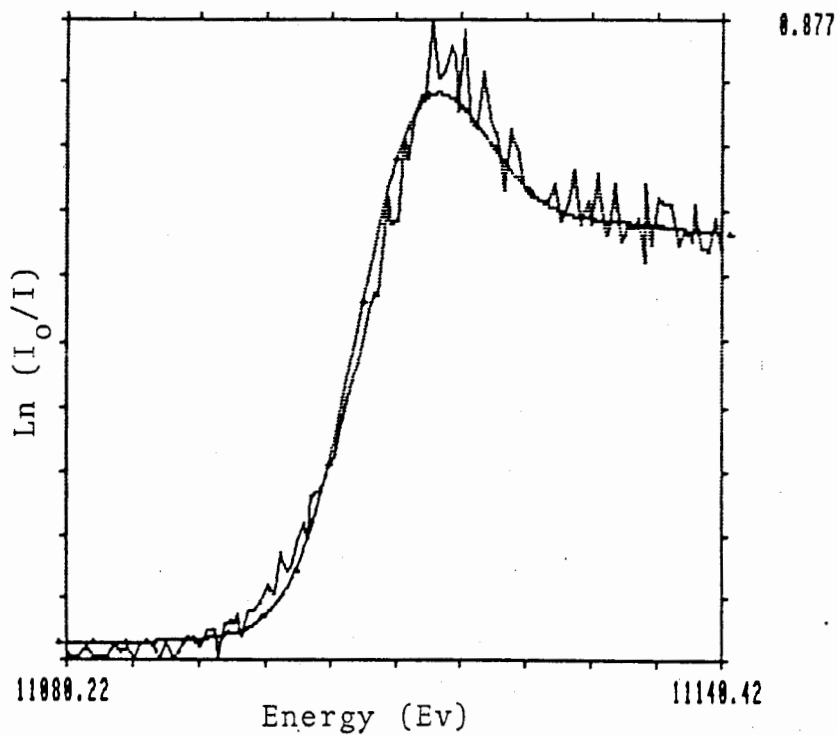
Fig. 4.1: *By using a Gaussian convolution function, the white line of amorphous Ge spectrum taken at SSRL is convolved to a similar spectrum taken at SFU.*

The white-line spectrum of amorphous Ge measured at SSRL (assumed to contain little or no smearing from finite energy resolution) was convolved with the resolution function (4.9), and τ was varied until agreement was obtained with the spectrum measured at our laboratory (See Fig. 4.1).

Fairly good agreement between the two curves was obtained for $\tau=5.4$. This confirmed the Gaussian as an adequate description of the resolution function. The FWHM value of the resolution is $2(2\ln2)^{1/2}\tau = 12.72$ eV.

Several authors [Knapp *et al.*, 1978 ; Cohen *et al.*, 1980; Khalid *et al.*, 1982; Georgopoulos and Knapp, 1981; Zschornack, 1982] have discussed how to calculate the energy resolution from the geometrical arrangement.

From the equation derived by Knapp *et al.* and Khalid *et al.* (see Appendix for details), the FWHM range $\Delta\theta$ about the mean angle θ is stated:

$$\Delta\theta = [8R \sin\theta]^{-1}\{(W_a + W_s)^2 + [(2 \ln 2 \cos\theta \sin\theta)/\mu]^2 + (h^2/8R \cos\theta)^2\}^{1/2}, \qquad (4.11)$$

where W_a is the projected width of the anode image, W_a is the width of the receiving slit, μ is the absorption coefficient of the crystal, h is the height of the anode image and the receiving

slit, R is the radius of the Rowland circle and θ is the angle of diffraction.

In our laboratory the width of the anode is 1 mm, with take-off angle 8°, W_{α} is 0.99 mm; $W_{\bullet}$ is 0.24 mm; h is 15 mm; R is 354 mm. At energy 11.1 KeV, μ crystal is 74.95 cm^{-1} [McMaster *et al.*, 1969] and θ is 32.4°. By using these figures, $\Delta\theta$ is 8.1479×10^{-4}. From equation (4.11) the energy resolution is 14.24 eV. This calculation agrees with the energy resolution obtained from experiment and processed by convolution.

The energy smearing can affect the determination of the structural parameters (the coordination number and the Debye-Waller factor), and hence the EXAFS spectrum must be corrected. Lengeler *et al.* have worked on this correction by convoluting the theoretical expression in equation (1.1) for the EXAFS interference function $\tilde{\chi}(k)$ with the resolution function (4.10) :

$$\chi(k) = \int_{-\infty}^{\infty} \tilde{\chi}(k') \, h(k,k') \, dk', \qquad (4.12)$$

The sine factor in equation (1.1) creates the strong variations of $\chi(k)$, whereas the other factors are slowly varying functions of k. By extracting the prefactors from the integral in equation (4.12)

and convoluting only the sine, and taking into account that the main k-dependence of the argument of the sine function is from $2kr_j$ and from the linear term of $\delta(k)$, Lengeler et al. have been able to solve the integral analytically. The result of the convolution is

$$\chi(k) = \sum \frac{N_j}{kr_j^2} \exp(-2\sigma_j^2 k^2) \exp(-2r_j/\lambda_j(k)) \times$$

$$F_j(k) \times \sin[2kR_j + \delta(k)) \times$$

$$\exp[-(2r_j + \alpha_j)^2 m^2 \tau^2 / 2\hbar^4 k^2] \qquad (4.13)$$

The finite-energy resolution (the monochromator energy resolution) shows up as an exponential damping factor:

$$M(k) = \exp[-(2r_j + \alpha_j)^2 m^2 \tau^2 / 2\hbar^4 k^2] \qquad (4.14)$$

This correction factor is discussed in detail in the next chapter.

4.2. Liabilities and Limitations

4.2.1. Energy Range

The energy range of the spectrometer depends on several factors, the most obvious of which is the geometrical constraint of the spectrometer. Based on equations (2.2), (2.5) and (2.6), the

energy range can be calculated.

Without the presence of the telescopic shielding, x_c (the crystal position) can travel from the position 170 mm (this minimum distance being limited to 280 mm if the telescopic shielding is installed) to 500 mm, x_1 can travel from -55 mm to 280 mm, y_1 can travel from -7 mm to position 580 mm, while θ can rotate practically 360 degrees (see Fig. 2.9).

The Rowland circle radius is 354 mm, so from equation (2.2) the range of θ is 13.89° to 79.8°, but equation (2.5) restricts the maximum of θ (based on the minimum value of x_1) to 47.71°. Based on this θ range, the energy range covered by the monochromomator using Si(111) is 2.677 - 8.251 keV and by using Si(333) is 8.032 - 24.75 keV.

However, for the initial work described in this thesis, it was decided that the radiation protection for personnel was very important; thus, the telescopic shield was constructed and installed between the x-ray housing and crystal holder. With the presence of this shielding, x_c is limited to the minimum value of 280 mm, and as a result, the energy range covered by this configuration is limited to 3 - 5.9 keV for Si(111) and 8.03 - 15.03 keV for Si(333).

With the crystal used in the present work, the x_c movement is not

so sensitive to the intensity recorded by the ionization chamber; this insensitivity spans 100 mm. This means that x_c can be set to the minimum 180 mm, and as the result, the θ has the minimum value 14.7° . Based on this new scheme, the energy range covered by the monochromator using Si(111) is 3 - 7.81 KeV and by using Si(333) is 8.032 - 23.4 KeV.

4.2.2. Sample Considerations

The sample should be homogeneous, and of uniform thickness with no pinholes. Any variation in the effective sample thickness will lead to a distortion of the EXAFS, which takes the form of an apparent decrease in the EXAFS amplitude [Stern and Kim, 1981; Goulon et al., 1982]. Significant distortions in EXAFS amplitude occur when $\mu_s x_s \geq 1.5$; therefore, even though the optimum total sample thickness as determined by statistical considerations is $\mu_s x_s = 2.55$, the thickness effect will introduce errors in the amplitude.

To ascertain whether the thickness effect is insignificant, several measurements of EXAFS can be made as a function of thickness. If the EXAFS does not change significantly as the thickness is varied, the effect is negligible. In practice, one must be suspicious of any EXAFS measurements made on a sample with an edge step thickness greater than 1.5, unless explicit tests have been made for the thickness effect [Stern, 1981].

Powdered samples are commonly used in EXAFS measurement because many materials can be prepared thin enough for transmission EXAFS by powdering and applying the powder in a thin layer. However, it is obvious that each particle in the sample exposes varying thickness to the beam — even if the powder were completely composed of one size of particle, the beam would sense a spread of thickness — therefore the particle diameter D should be very small, $\mu D \approx 0.1$ [Stern, 1981; Goulon et al., 1982; Crozier et al., 1987]. The cross-sectional area of the x-ray beam should be less than that of the sample and should be defined by appropriate masks preceding the I_o chamber.

Solid samples with the required thickness can usually be obtained as evaporated or sputtered films, as foils or as finely ground powder.

4.2.3. Form of experiment

The experiment which has been done in the laboratory was a transmission EXAFS experiment (in which the second detector is placed directly behind the sample). This apparatus could also be used to acquire EXAFS data in the fluorescent mode or other forms. The core hole that is created by the photoabsorption process can decay by either a radiative or a nonradiative transition, as illustrated in Fig. 4.2.

69

In radiative decay, a higher-lying electron fills the core hole with the emission of a photon of energy $\hbar\omega_f$, equal to the difference in the two energy levels. This fluorescent photon energy is characteristic of the atomic transition that fills the core hole and is therefore independent of the incident photon energy. The intensity of the fluorescent yield is proportional to the probability that the incident photon has created a core hole; that is, it is proportional to the absorption coefficient. Thus the fluorescence will exhibit EXAFS.

In this kind of EXAFS experiment, the fluorescent radiation at $\hbar\omega_f$ is monitored as a function of the energy of the incident radiation absorbed in the sample. The resulting fluorescent radiation is monitored by a detector placed at 90° to the incident beam to reduce the contribution of scattered radiation [Sandstrom and Fine, 1980; Hayes and Boyce, 1982]. The position of the first detector (I_o detector) is similar to that in a transmission experiment.
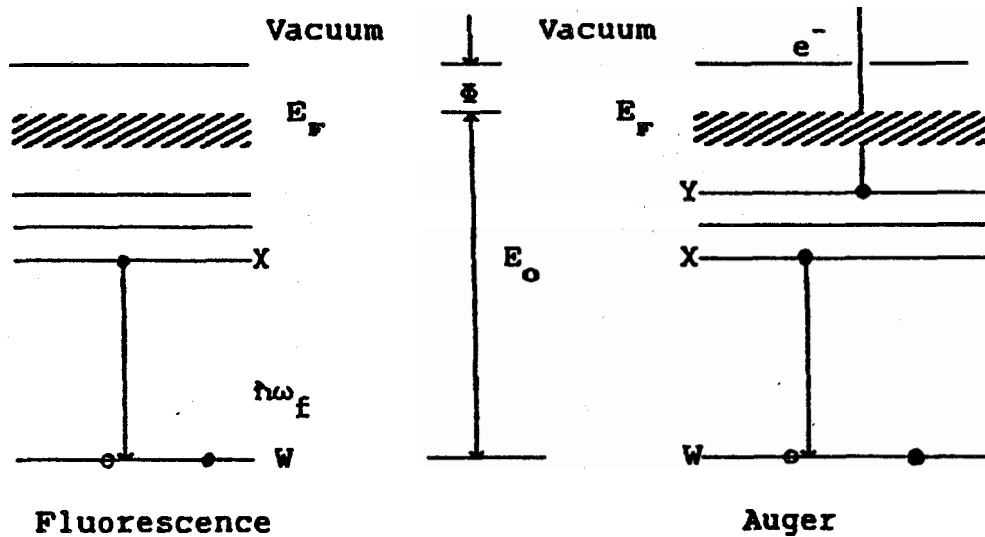
Fig 4.2. *The two processes by which the core hole created in the photoexcitation process can decay. In radiative decay, a fluorescent photon is emitted with an energy equal to the difference in the two energy levels,* $\hbar\omega_f = E_x - E_v$ *(W is the lower energy level containing the core hole and X is the energy level from which the de-excitation occurs). In the nonradiative decay process, an Auger electron is emitted to take up the energy from the* $X \longrightarrow W$ *transition.* Φ *is the ionization energy.*

71

Chapter 5

Application

5.1. Sample

As indicated in chapter 4, section 4, the sample should be homogeneous, and of uniform thickness with no pinholes. Any variation in the effective sample thickness will lead to a distortion of the EXAFS, which takes the form of an apparent decrease in the EXAFS amplitude. This will affect determination of the coordination number and the peak width, but will not seriously affect near-neighbour spacing [Hayes and Boyce, 1982].

The EXAFS spectra of crystalline and amorphous germanium have been measured in our laboratory. The amorphous germanium in this investigation was two thin layers (each layer 24 μm) deposited on Kapton by evaporation from a graphite boat using an electron beam in a vacuum better than 2×10^{-6} Torr. The crystalline germanium was ground with mortar and pestle to make a fine powder. The powder was rubbed by hand on the sticky side of transparent Scotch tape, then formed into several layers. The thickness of the sample was checked by measuring the absorption of Ge above the edge (at

11.104 keV). It was measured that 3 layers of sample has an absorbance (μx) $\approx$ 0.557.

5.2. Experimental Results and Analyses

Figure 5.1a shows the EXAFS spectrum of amorphous germanium. The data was averaged over five scans, each scan consisting of 112 points, namely 4 points in the pre-edge, 15 points in the edge, and 92 points in the post-edge regions. The integration time of each point was 60 seconds. Each scan took approximately two hours.
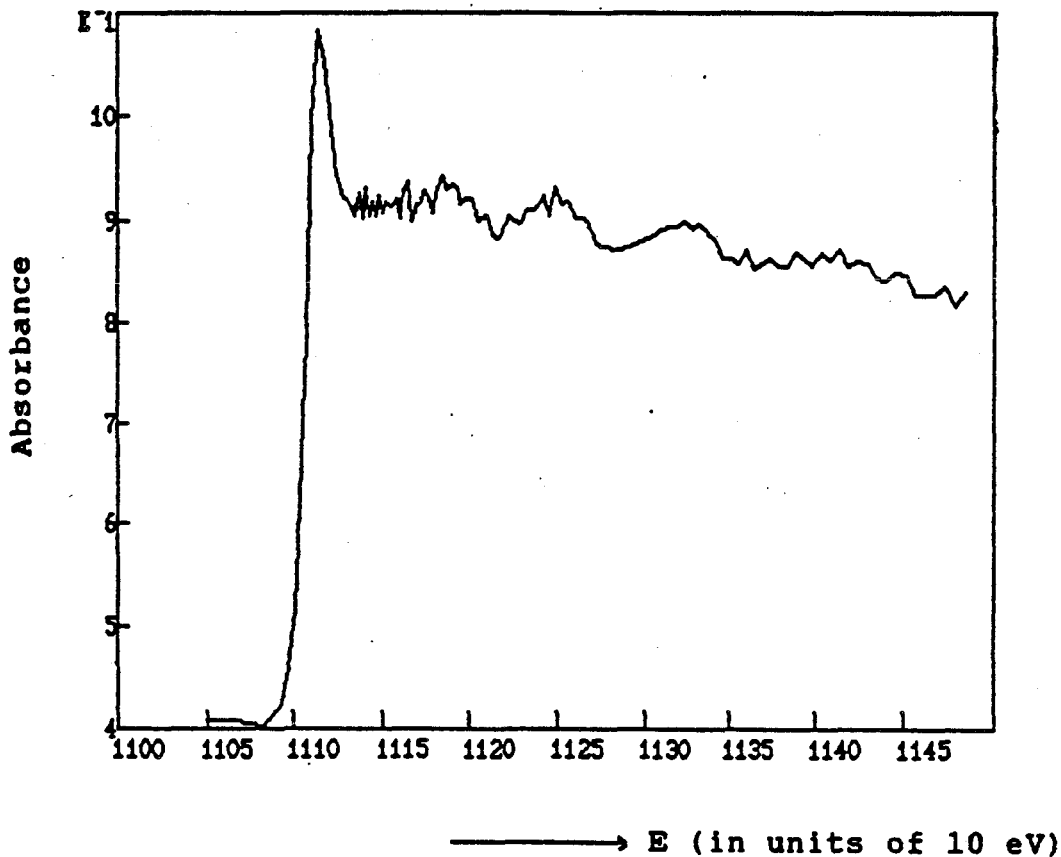

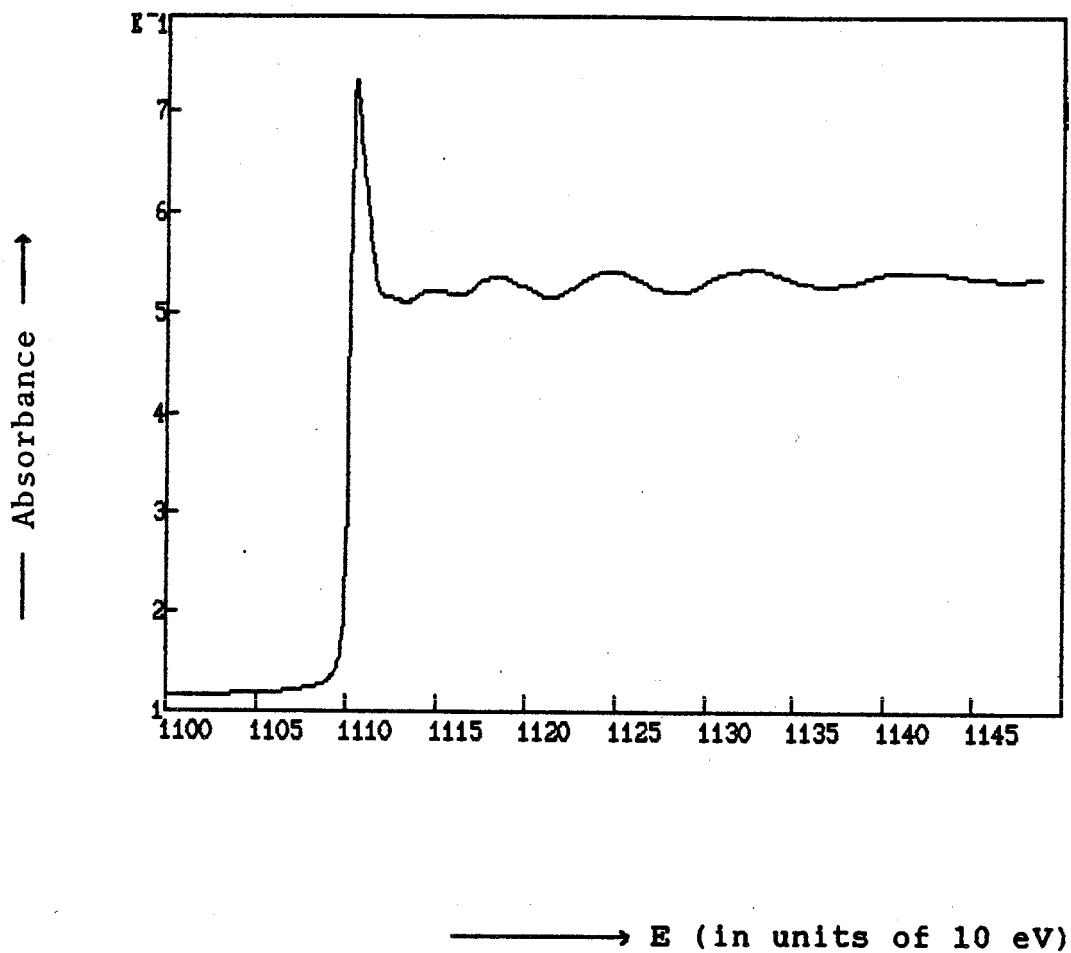Fig. 5.1a: *Absorbance as a function of photon energy of x-rays for amorphous Ge obtained at SFU.*

Fig. 5.1b: *Absorbance as a function of photon energy of x-rays for amorphous Ge obtained at SSRL.*

As a comparison, Fig. 5.1b shows the absorbance as a function of photon x-rays for amorphous Ge obtained at SSRL. The data were taken within 7 minutes.

Figs. 5.1a and 5.1b show the natural log I_o/I vs. energy, which is related to the absorption coefficient μ by the equation $I = I_o e^{-\mu x}$, where x is the sample thickness. The figures show the substantial increase in the absorption as the incident photon energy is increased past 11.1 keV, which marks the onset of absorption due to photoexcitation of electrons from the Ge K-shell.

The EXAFS is manifest as sharp oscillations in the absorption cross section above the K-edge. These oscillations have been shown to contain considerable information about the local environment of the excited-atom species [Sayers et al., 1971; Stern et al., 1975; Asheley and Doniach, 1975; Lee and Pendry, 1975; Hayes et al., 1976; Crozier et al., 1977; Lee et al., 1981].

All analyses of the EXAFS region of the spectrum start with the basic equation stated in (1.1):

$$\chi(k) = \sum_j \frac{N_j}{kR^2_j} \, S^2_o(k) \, |f_j(k,\pi)| \, \sin\left[2k \, R_j + \delta_j(k)\right] \times$$
$$e^{-2\sigma^2_j k^2} e^{-2R_j/\lambda_j(k)} \qquad\qquad (5.1)$$

Given a set of data and the basic EXAFS equation (5.1), there are clearly a large number of approaches for extracting distances and information about phase shifts, the amplitudes, and the Debye-

Waller factors. One of the earliest analyses [Sayers *et al.*,1971] was based on the Fourier transform of the data expressed in photoelectron momentum space. The absolute value of the transform was found to peak at distances shifted from the known values by several tenths of angstroms. Later on Lytle, Sayers and Stern [1975] corrected this shift using systems with known distances to extract bond lengths. Citrin *et al.* [1976], for a simple system, extracted the phase function $\delta(k)$ by direct curve fitting to equation (5.1) to show that this function could be transferred to other simple systems to extract bond lengths with an accuracy of 0.01 to 0.02 Å. This approach, however, is not generally applicable to systems of more than one principal distance. The two methods of Fourier transform and curve fitting have been combined to analyze more complicated systems. The curve fitting is carried out either in Fourier r-space [Hayes *et al.*, 1976] or in k-space by backtransforming of a certain shell [Crozier and Seary, 1980; Lee *et al.*, 1981].

Teo and Lee [1979] have calculated the EXAFS amplitude and phase function from first principles (using a small atom scattering theory) for K- and L-edges of nearly half of the elements in the periodic table. These theoretical EXAFS functions can be used to avoid the tedious task of searching, measuring, and analysing model compounds. In this thesis work, two methods to extract the structural information are used: curve-fitting with Teo and Lee calculations [Crozier and Seary, 1980] and comparison with SSRL

results.

In applying equation (5.1) (see chapter 1 for the meaning of all symbols), two general material-dependent factors must be considered (Brown and Doniach, 1980):

a. the mean electron density of the absorber environment, which determines the importance of multiple scattering effects; and

b. the degree of coordination order, determining the nature of the distribution function P(R) (see equation (1.3)).

Point (a) determines a fundamental physical limitation, i.e. the lower bound on the range of the photoelectron k-vector, k_{min}, below which multiple scattering effects become important and where equation (5.1) fails. In practice, k_{min} is usually determined empirically for a given class of materials. For instance, in earlier works on EXAFS, in organic molecules (where the absorber environment has low Z and low coordination number) k_{min} was usually set in the region of 3 $Å^{-1}$ (corresponding to photoelectron energies of about 35 eV). On the other hand, for dense material, such as metallic Cu, it has been argued that multiple scattering effects may well be important to 300 eV (about 9 $Å^{-1}$) leading to a much more restricted range of validity for (5.1) (Ashley and Doniach, 1975). However, recently it has been shown theoretically (Muller and Schaich, 1983; Schaich, 1984) that a single scattering approach can be used to calculate the final state in x-ray absorption, which means k_{min} can be set lower. Furthermore, Bunker

and Stern [1984] have shown experimentally that the effects of multiple scattering at low k are much smaller than had been thought. In particular, in analysing amorphous materials, the crystalline counterpart provides an excellent reference; the empirical amplitude and phase shift can be transferred because the multiple scattering effects are basically the same in crystalline and amorphous material. This opens up prospects for using the $\chi(k)$ data down to $k \approx 1 \text{ Å}^{-1}$ [Bunker and Stern, 1984]. The upper value of the k range, k_{max}, is usually determined by the data itself. The value of k_{max} depends strongly on experimental considerations, dilution of absorber species, available photon counts, etc. In practice, values of k_{max} range from 11 to 22 Å^{-1}.

Point (b) determines the nature of physical information to extract from EXAFS data, information about shell-coordination distances, backscattering amplitudes, phase shifts, etc. For polycrystalline and molecular material, P(R) consists of a series of well-defined coordination shells whose atomic constituents are in general disordered as to orientation (except in single-crystal samples) but very well defined as to distance. For amorphous or liquid samples, on the other hand, both angle and interatomic distances are disordered so that P(R) must be represented by a continuous distribution rather than a series of δ-functions as in the crystalline and molecular case [Crozier and Seary, 1980; Crozier *et al.*, 1987].

5.2.1. Removal of Background Absorption

It is convenient to regard the total experimental absorption cross section as the sum of two distinct contributions: the Ge K-shell absorption cross section μ, which contains the EXAFS information, and a slowly varying background absorption μ_o. This background absorption is due to the photoexcitation of those electrons in the system which are less tightly bound than the K-electrons of interest in this case. As obtained experimentally, the pre-threshold absorption also includes energy-dependent contributions from the x-ray photon counter, the sample holder, and so on [Crozier and Seary, 1980; Hayes and Boyce, 1982].

Normally, the first step in data reduction is to subtract the background due to excitation of higher shells by using a Victoreen fit (or some functional form) [Lytle *et al.*, 1975] of the form $\mu' = C\lambda^3 - D\lambda^4$, where λ is the x-ray wavelength and C and D were found by fitting this formula to the measured absorption curve on the lower-energy side of the edge, yielding $\mu(E)x$, the total absorption of the K-shell of the sample of thickness x (see Fig. 5.2). If there is large noise involved, then the data is smoothed before any other analysis; *i.e.*, the data points are weighted so that unwanted noise in the data is averaged. Given a set of data $(x_1, x_2, x_3, \ldots x_n)$ corresponding to data $(y_1, y_2, y_3, \ldots y_n)$, new data is formed [Seary, 1987]:

$$Y_{nev} = Y_1, \ldots, 0.5 \left[y_i + \frac{(x_i - x_{i-1})y_{i+1} + (x_{i+1} - x_i)y_{i-1}}{(x_i - x_{i-1}) + (x_{i+1} - x_i)} \right], \ldots, Y_n$$

$$(5.2)$$

The general term reduces to

$$y_i^{nev} = .5 \ y_i + .25(y_{i-1} + y_{i+1})$$

when $x_i - x_{i-1} = x_{i+1} - x_i$ (the data step is constant).

The data is then converted from energy space to momentum space (k) according to equation (1.2):

$$k = [\ 2m(E - Eo)/\hbar^2 \ ]^{1/2},$$

$$(5.3)$$

where E_o is the threshold energy. There is no simple relation between features in the experimental spectrum and E_o as defined by equation (5.2) because several complicated physical processes such as chemical bond effects and core relaxation affect these features near the threshold [Stern et al., 1975]. At first approximation, E_o is arbitarily fixed at a special feature in the spectrum (at a point of inflection). Later on, for further analysis, E_o can be made an adjustable parameter to compensate for the inadequacies of the simple EXAFS formula and permit the use of a wide range of model compounds or calculated phase shifts in determination of distances.

80
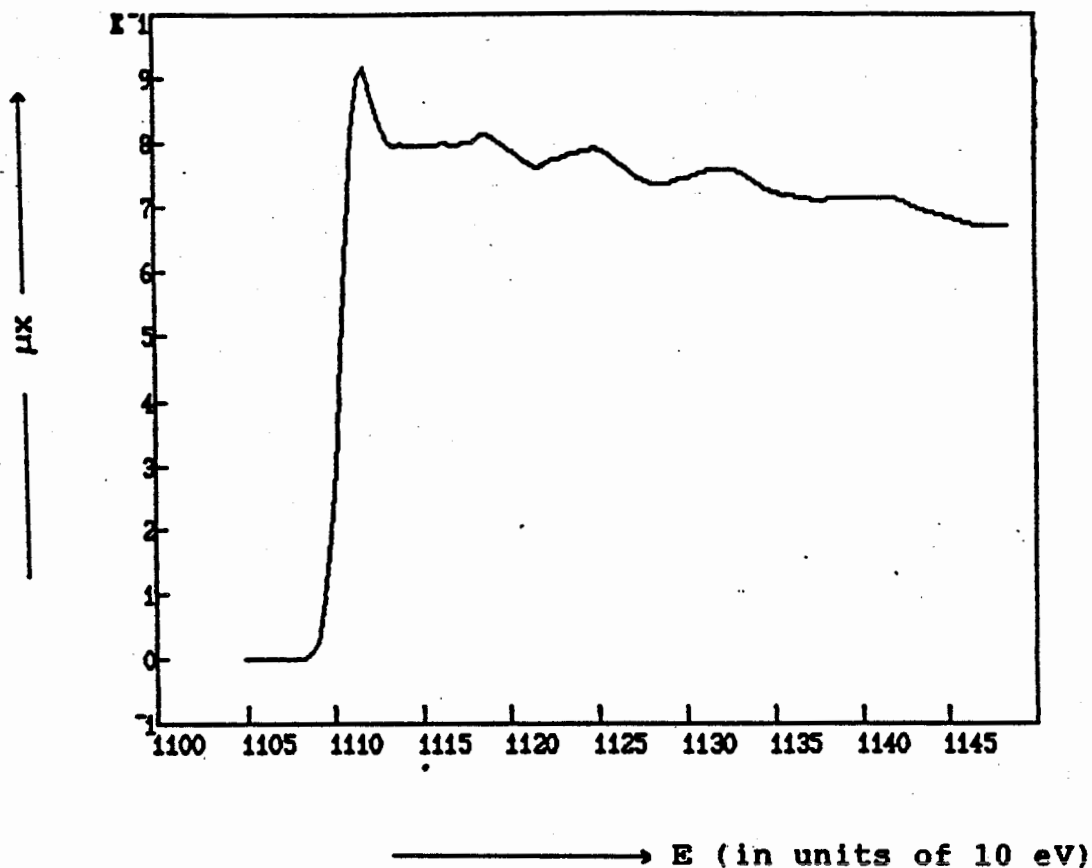
Fig 5.2: *K-shell absorbance (μx) as a function of photon energy of x-rays for amorphous Ge. The data was smoothed prior to pre-edge removal.*

5.2.2. Extraction of the EXAFS Interference Function $\chi(k)$

The next step is to obtain $\mu_o(k)$, the slowly varying function of $\mu(k)$ above the edge. A low-order polynomial is fitted to $\mu(k)k^n$ by a least-squares procedure. This fit has the effect of averaging out EXAFS modulations, so that on subtracting the resultant from

81

data, the residual modulations oscillate rather evenly about zero. In all cases the fit was restricted to the EXAFS range that was to be used in the final structural analysis. Finally, the resulting background-subtracted data may be normalized to a per-atom basis by dividing by the background-fit function at each value of k, yielding an empirical evaluation of the EXAFS modulation function $\chi(k)$.

$$\chi(k) = (\mu(k) - \mu_o(k))/\mu_o(k) \tag{5.4}$$

However, dividing by $\mu_o(k)$ at each k may cause some problems if $\mu_o(k)$ is not highly smoothly varying. In this case, the normalization is done by scaling $\chi(k)$ to the jump in the absorption coefficient at the K-edge energy and using the McMaster table [1969] fits to remove the k-dependence of the background absorption above the K-edge [Crozier and Seary, 1981].

$$\chi(k) = \frac{(\mu(k)x - \mu_o(k)x)}{\text{Edge jump}} \times \frac{\mu(0)^{\text{McMaster}}}{\mu(k)^{\text{McMaster}}} ,$$

where the edge jump, $\mu(0)x$, is measured at k=0 from the lowest point of the absorption spectrum to the mid-point of the oscillation (see Fig. 5.2).

Fig. 5.3 shows the EXAFS interference function $\chi(k)$ for amorphous germanium.

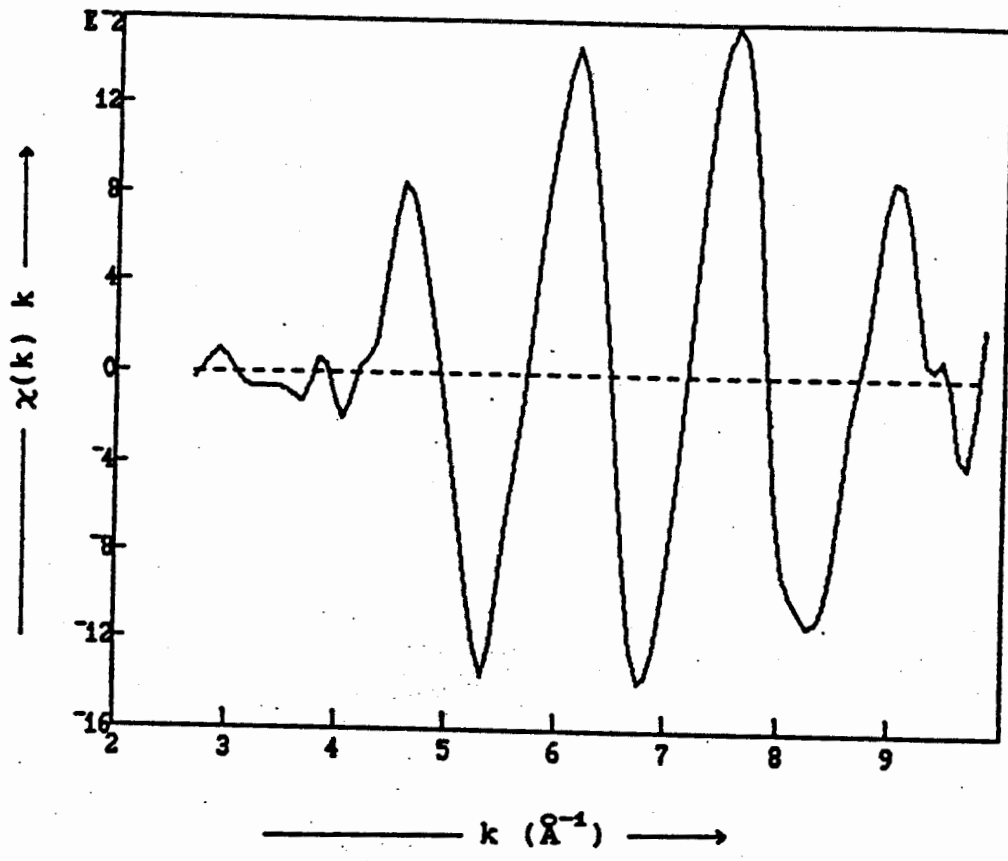Fig. 5.3. *Normalized χ(k) versus k plots for amorphous Ge*

5.2.3. Fourier Transform into R-space

The next step in the EXAFS analysis is a Fourier transform of the EXAFS function yielding a radial structure function (RSF), $\Phi(R)$. This isolates the contributions of the different shells of neighbours and allows the use of filtering techniques to remove much of the noise and to study each shell separately.

$$\Phi(R) \quad = \quad \int_{k_{min}}^{k_{max}} k^n \; W(k) \; \chi(k) \; \exp \; (-2ikR) \quad dk \qquad (5.5)$$

where k^n is a k-weighting term to compensate for the diminishing amplitudes at high k-values, k_{min} and k_{max} are the minimum and maximum values of k specifyng the range of the transform. $W(k)$ is a Gaussian window function [Crozier and Seary, 1980] used to suppress transform artefacts. The function is centered about the k-space range and decreases to 10% at the ends of the range.

The interference function $\chi(k)$ is the sine transform of the pair distribution function $P(R)$ (see equation (1.3)); thus,to recover $P(R)$ the inverse sine transform should be taken. However, because of the finite range of the data, particularly the truncation at low values of k, the inverse sine function is a rapidly oscillating function from which it is difficult to assign peaks to bond lengths. Consequently it is convenient to take a complex transform and examine its magnitude. For systems in which $P(R)$ is Gaussian, the interatomic distance is then determined from the position of the peak in the magnitude of the transform [Crozier and Seary, 1980]. Use of the magnitude avoids the need to have a quantitative knowledge of $\delta(k)$; the effective shift in the peak position due to $\delta(k)$ is calibrated by a reference compound (from the EXAFS data of a known structure which has a similar chemical
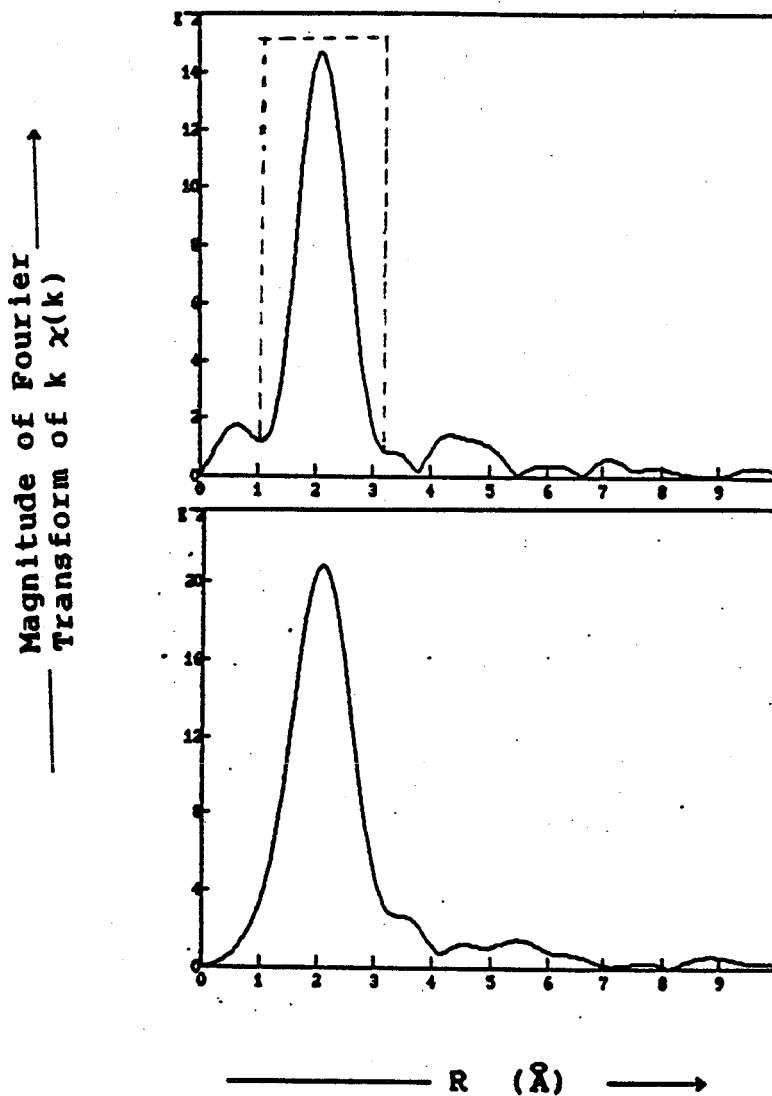
Fig 5.4. Magnitude of Fourier transform of $k\chi(k)$ data

(a) for amorphous Ge, $k_{min} = 3.38 \ \overset{o}{A}^{-1}$ and $k_{max} = 9.83 \ \overset{o}{A}^{-1}$

(b) for crystalline Ge, $k_{min} = 3.68 \ \overset{o}{A}^{-1}$ and $k_{max} = 9.83 \ \overset{o}{A}^{-1}$

The phase shift has not been included and a Gaussian Window function (10% at k_{min} and k_{max}) was used.

environment) or is fitted using theoretical calculations. Fig. 5.4 shows the magnitude function of the EXAFS RSF.

The large peak at $\approx$ 2.2 Å is the result of the contribution from the first shell of Ge neighbours. Other smaller peaks visible at larger distance are due to noise rather than to more distant neighbours. The Fourier transform peaks at an apparently lower distance than the known crystallographic distance of 2.45 Å due to the effect of the phase shift $\delta(k)$.

5.2.4. Curve Fitting

In order to determine the structural parameters of a given shell, a curve-fitting analysis was performed. The first step in the curve-fitting procedure is to process the EXAFS interference function $\chi(k)$ by a Fourier filtering technique, which consists of Fourier-transforming the data (actually $k\chi(k)$ vs. k) into R-space, selecting the distance range of interest with a square window, and retransforming back to k-space. The dashed line in Fig. 5.4 is a square window function for isolating the first shell EXAFS. In the transformation, the Gaussian window in k-space is removed by dividing by $W(k)$.

Using the calculation of $\delta(k)$ by Teo and Lee [1979], the origin of the total phase shift was shifted by varying E_o until obtaining the best straight line (in the least squares sense) passing

through the origin. The values of E_o were found to be -0.05 eV and 0.87 eV for amorphous and crystalline germanium, respectively.

The amplitude of equation (5.1) can be written as:

$$A(k) = \frac{N}{kR^2} T(k) \; e^{-2\sigma^2 k^2} , \qquad (5.6)$$

where

$$T(k) = |f(k)| \; e^{-2R/\lambda} S_o^2(k) \qquad (5.7)$$

A first approximation to $|f(k)|$ is obtained by interpolation of the calculations of Teo and Lee [1979]. For first shells, inelastic effects are included in $|f(k)|$. The factor $S_o^2(k)$ is assumed to be a constant, so that N must be obtained from a reference compound.

The quantity $\ln \left(\dfrac{k \, A(k)}{T(k)} \right)$ was least-squares fitted to k^2 over a certain linear region (see Fig. 5.5). From fitting, the values N and σ^2 can be deduced. Fitting over the range 5.67 - 8.5 $\overset{o}{A}{}^{-1}$ for amorphous germanium gave the results N = 2.99 ± 0.1 and σ^2 = 0.0064 ± 0.002 $\overset{o}{A}{}^2$; and over the range 5.22 - 8.52 $\overset{o}{A}{}^{-1}$ for crystalline germanium gave N and σ^2 to be 3.57 ± 0.9 and 0.0046 ± 0.0025 $\overset{o}{A}{}^2$, respectively.
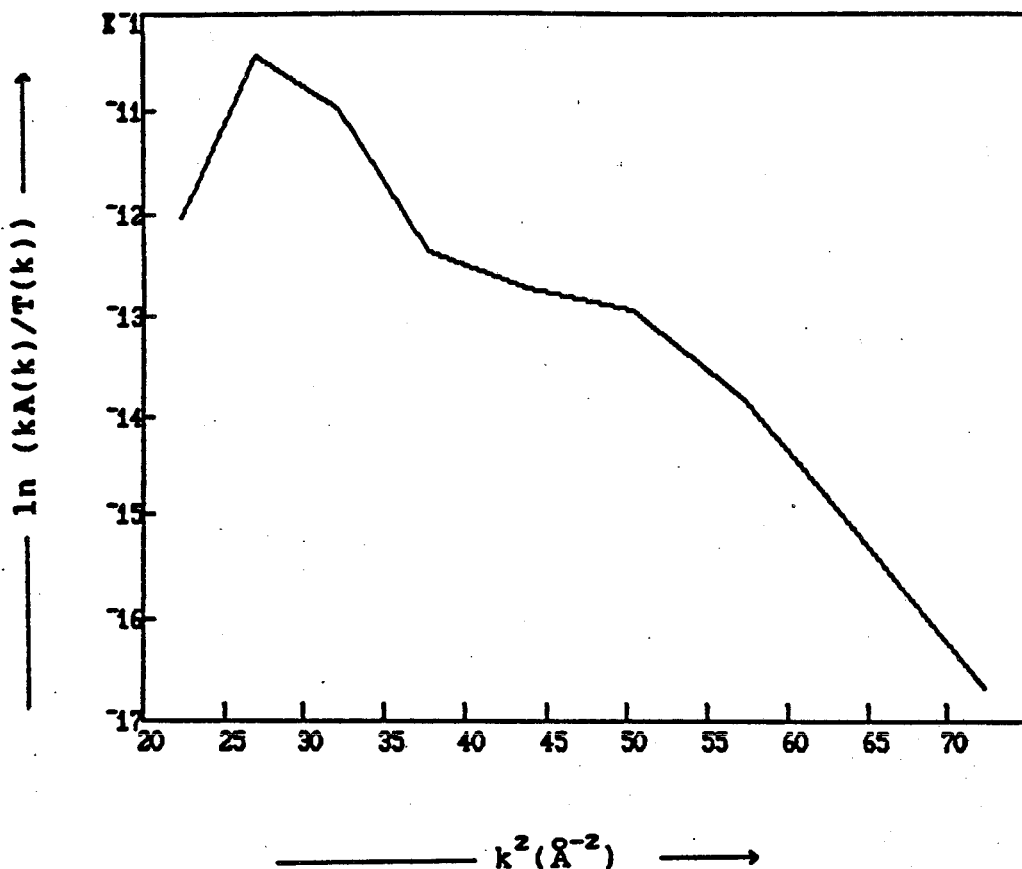
Fig. 5.5: *Plot of* ln (kA(k)/T(k)) *vs.* k^2 *to obtain the coordination number and the Debye-Waller factor of amorphous Ge.*

Fig. 5.6 shows the comparison of the interference function $\chi(k)$ obtained from experiment and the fitted value by using the theoretical calculation of Teo and Lee [1979]. The two curves show fairly good agreement over most of the k region. At lower k the curves do not fit well because the theoretical calculation is

intrinsically incorrect at low k [Crozier and Seary, 1981].
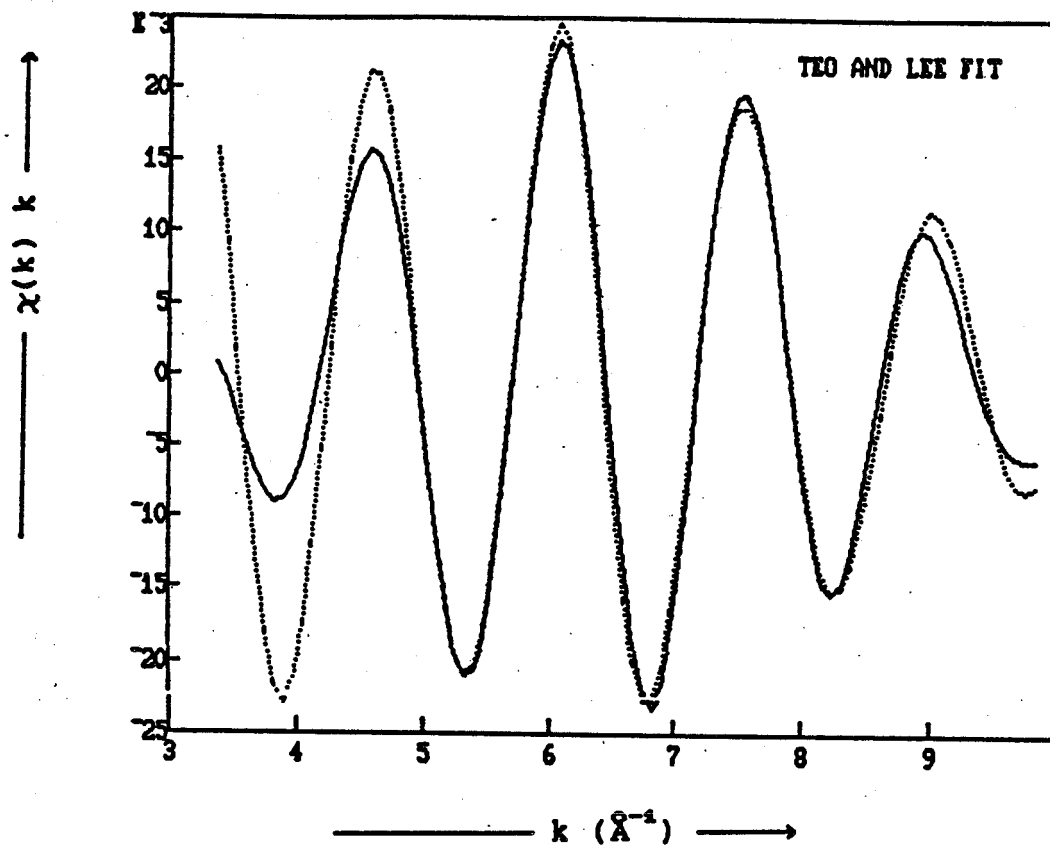
Fig 5.6: *Comparison of the EXAFS interference functions. The solid line shows the data, the broken line shows the theoretical fit.*

The values of E_o obtained from the fitting were used to modify the original data of the EXAFS interference function, by shifting the origin of the k scale. The function was then transformed to real space to obtain the nearest atomic distance. In taking the transform, the phase shift $\delta(k)$ obtained from the fitting was removed. The nearest atomic distances for amorphous and crystalline germanium were found to be 2.444 ± 0.01 Å and 2.425 ±

0.01 Å, respectively. The monochromator resolution affects the amplitude of $\chi(k)$ and not its phase, so these values for the interatomic distances are accurate. However, the values of N and σ^2 are in error because the monochromator resolution function has not yet been included.

5.2.5. Data Comparison

Assuming that chemical transferability is valid (the back scattering amplitude and the phase shifts are the same for an atom which has similar chemical environment), the structural information can be obtained by comparing data to a known reference.

The data obtained in our laboratory were compared to reference data (crystalline germanium) obtained in SSRL. From equation (5.1), the amplitudes can be compared as follows:

$$\ln \left(\frac{A(k)_{sfu}}{A(k)_{ssrl}} \right) = \ln \left\{ \frac{N_{sfu}}{N_{ssrl}} \left(\frac{R_{ssrl}}{R_{sfu}} \right)^2 \right\} - 2(\sigma^2_{sfu} - \sigma^2_{ssrl}) \, k^2$$

$$(5.8)$$

The phase shifts can be compared:

$$\psi(k)_{sfu} - \psi(k)_{ssrl} = 2 \, k \, (R_{sfu} - R_{ssrl}) \qquad (5.9)$$

$$k^2 \ (\AA^{-2})$$
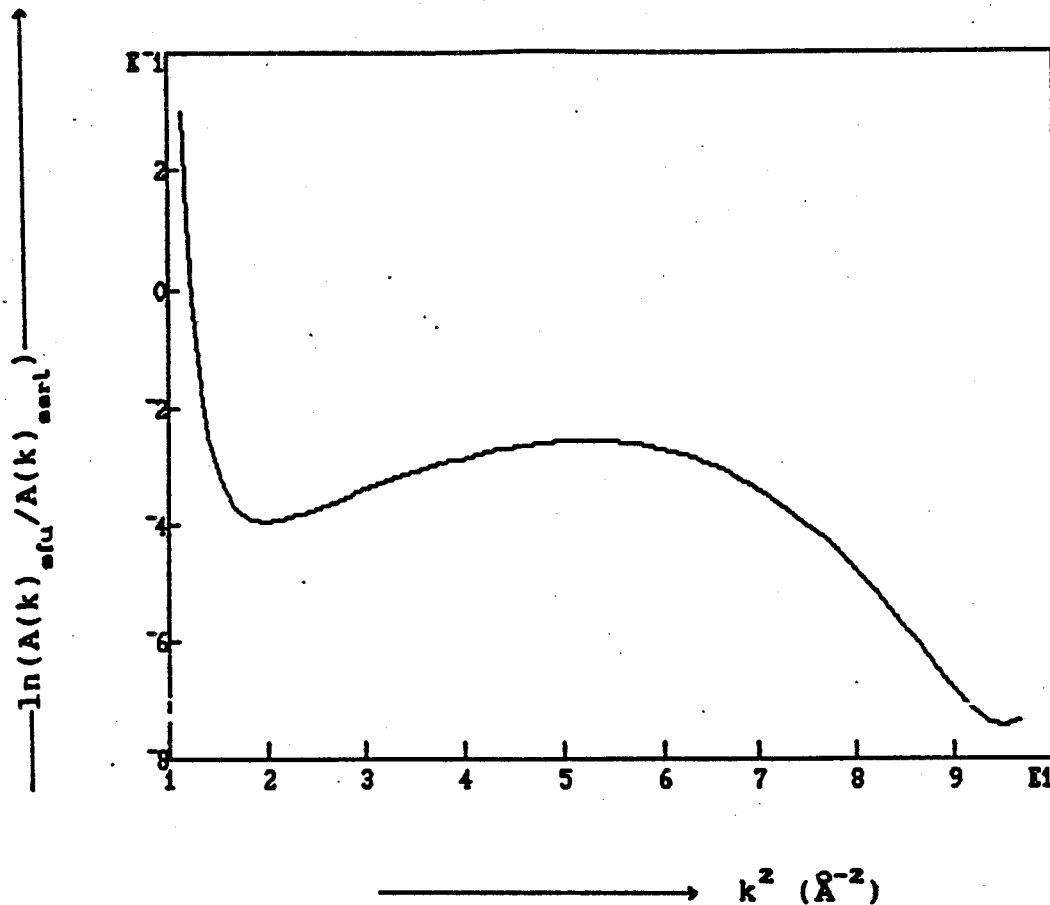
Fig. 5.7: *plot of* ln $(A(k)_{afu}/A(k)_{asrl})$ *vs.* k^2 *to obtain the coordination number and the Debye-Waller factor of amorphous Ge.*

Fig. 5.7 shows the plot of ln ($\dfrac{A(k)_{afu}}{A(k)_{asrl}}$) *vs.* k^2 of amorphous Ge from SFU data and crystalline Ge of SSRL data. From least-squares fitting over the region 4.65 - 9.53 $\AA^{-1}$, the difference of the Debye-Waller factors was found to be -0.0015 ± 0.0003 $\AA^2$, and the ratio of $\Delta C = (N_{afu}R^2_{asrl}/N_{asrl}R^2_{afu})$ was found to be 0.826 ± 0.054. Fitting equation (5.9) over the range 3.45 - 9.83 $\AA^{-1}$ gave the result $R_{afu} - R_{asrl}$ = 0.029 ± 0.002 $\AA$.

A similar comparison was done for crystalline germanium data

obtained at SFU and its counterpart obtained at SSRL. Over the fitting range 4.27 - 9.53 Å^{-1} it was found $\Delta C = 0.866 \pm 0.03$, $\sigma_{sfu}^2 - \sigma_{ssrl}^2 = -0.00045 \pm 0.0003$ Å^2 and, over the fitting range 3.68 - 9.83 Å^{-1} it was found $R_{sfu} - R_{ssrl} = 0.024 \pm 0.006$ Å.

Comparing with the SSRL results [Crozier and Seary, 1981], the value of σ_{sfu}^2 can be calculated, namely, σ_{sfu}^2 (amorphous Ge) is 0.00501 ± 0.00051 Å^2 and σ_{sfu}^2 (crystalline Ge) is 0.00395 ± 0.00048 Å^2. The interatomic distances for amorphous and crystalline germanium obtained using this method are close to the known crystallographic distance. When both SFU data were compared to each other, it was found: $\Delta\sigma^2 = 0.004 \pm 0.006$ Å^2 and $\Delta R = 0.012 \pm 0.003$ Å (amorphous to crystalline). The large error in $\Delta\sigma^2$ reflects the noise present in the two SFU data sets being compared.

The two methods of calculation (fitting with the theoretical calculation of Teo and Lee, and comparing with SSRL data as a reference) show that the coordination numbers of amorphous and crystalline germanium obtained at SFU are lower than the known value. The two calculations also indicate that the Debye-Waller factors of the data obtained at SFU are larger than those of their counterpart data obtained at SSRL. This is because the monochromator resolution, ΔE, at SFU is larger than that at SSRL. The finite resolution has the effect of decreasing the amplitude (see equation 4.14); the Debye-Waller factor σ^2 determined by the

fitting procedure increases. The effect is more pronounced at lower k, causing the coordination number found to be lower than the known value.

The monochromator resolution function is given by equation (4.14):

$$M(k) = \exp - (2R + \alpha)^2 m^2 \tau^2 / 2\hbar^4 k^2 \qquad (5.10)$$

If we assume that $\tau = 0$ for the SSRL double crystal monochromator at the Ge K-edge, then the instrumental broadening of SFU data is given by the equation:

$$\chi(k)_{sfu} = M(k) \; \chi(k)_{ssrl} \qquad (5.11)$$

Since the value of α can be obtained from the phase calculation of Teo and Lee, and the value of R has already been calculated in the previous section, then the value of τ can be calculated by fitting the data as in equation (5.11).

Fig. 5.8 shows the comparison between the EXAFS interference functions obtained at SFU (amorphous Ge) and SSRL (crystalline Ge). The SSRL data was convolved according to (5.11) for different τ until it matched the SFU data. A good agreement between the two curves was achieved on setting $\tau = 6.3$, meaning the energy resolution of the monochromator is 14.835 eV. The result is in good agreement with the other calculation indicated in chapter 4.
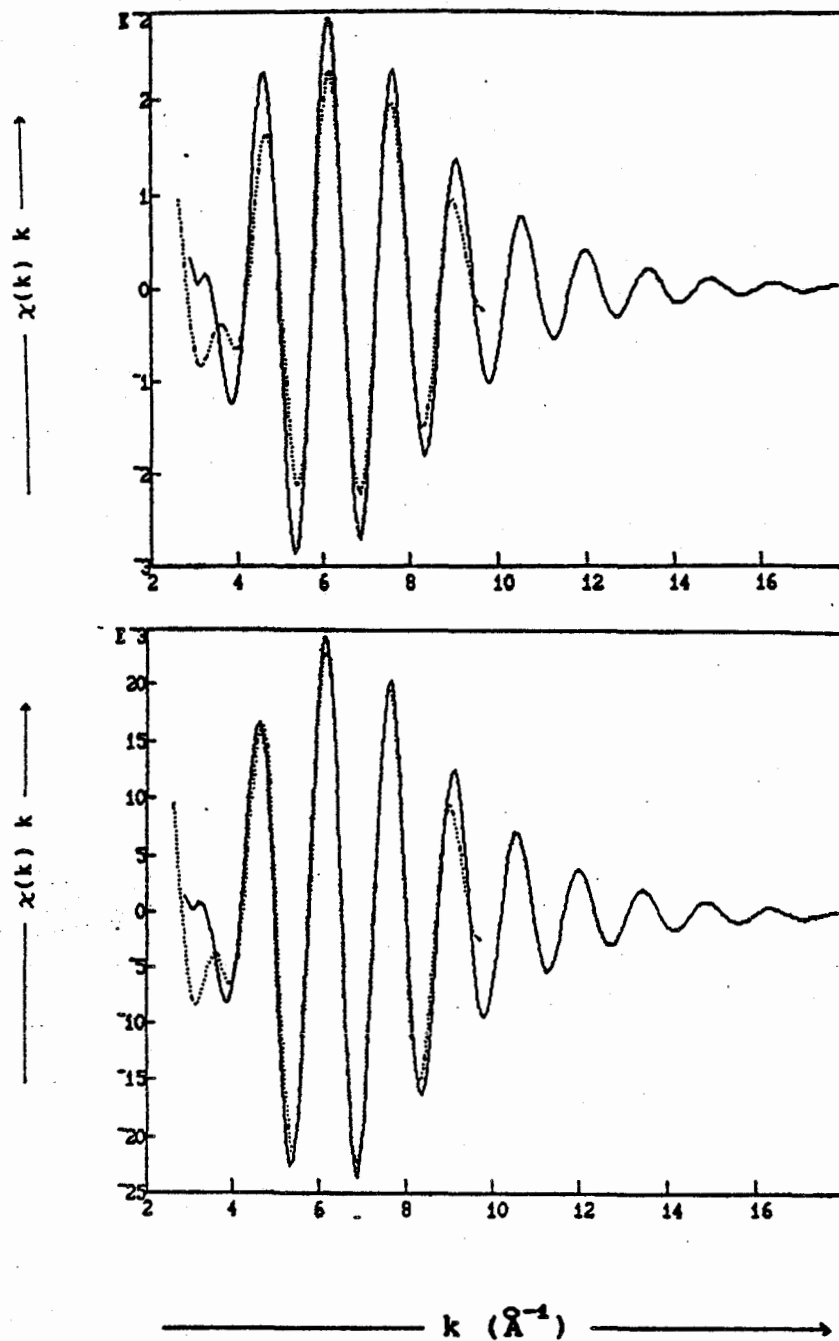
Fig. 5.8: Comparison between the EXAFS interference function of amorphous Ge (obtained at SFU, dashed line) and amorphous Ge (obtained at SSRL, solid line). The upper plot shows the data before convolution is applied. The SSRL data is then convolved by varying τ of the monochromator function function. The two curves reach a good agreement (lower plot) when τ is set to 6.3.

This convolution result also indicates that the quality of the Fourier filtered data obtained at SFU is relatively comparable with the result obtained at SSRL. The energy resolution of SFU data is worse than for the result from SSRL data, and causes deterioration in its amplitude and σ^2. By correcting with the monochromator resolution function, better values of amplitude and σ^2 can be recovered.

Finally, the experiments also show that the Debye-Waller factor of amorphous germanium is greater than that of crystalline germanium. This is due to the fact that the Debye-Waller factor can be separated from two contributions as follows (Sayers *et al.*, 1971):

$$\sigma^2 = \sigma_T^2 + \sigma_D^2 \qquad (5.12)$$

where T and D indicate thermal and structural disorder broadening, respectively. The thermal effect for the two kinds of germanium is the same, but amorphous germanium has greater structural disorder (Crozier and Seary, 1981).

Chapter 6

Conclusion

Synchrotron radiation, because of its unique properties of polarization, extremely high photon flux, and tunability, will continue to be the choice for EXAFS research. However, a great many EXAFS experiments can be performed successfully using alternate energy sources such as from a conventional x-ray generator with a water-cooled sealed tube or from a rotating anode x-ray generator.

This work has demonstrated that EXAFS spectra can be collected with our laboratory EXAFS facilities even though the x-ray intensity collected through a focusing crystal scheme is relatively low (10^4 - 10^5 photons/sec), the energy resolution is very broad (about 14 eV at 11 keV) and the detectors are noisy.

The nearest neighbour interatomic distance obtained in this experiment for crystalline germanium (2.425 ± 0.01 Å) is in good agreement with the known crystallographic distance 2.4498 Å [Cullity, 1978]. The nearest neighbour distance for amorphous germanium was found to be 2.444 ± 0.01 Å. In an earlier work using

synchrotron radiation [Crozier and Seary, 1981] the distance was found to be 2.45 ± 0.01 Å in amorphous germanium.

The Debye-Waller factors were found to be 0.0050 ± 0.0005 $Å^2$ and 0.0040 ± 0.0005 $Å^2$ for amorphous and crystalline Ge. The factor is larger for the amorphous material due to the structural disorder. The results compare favorably with other experimental values [Crozier and Seary, 1981] of 0.0035 ± 0.0002 $Å^2$ for crystalline germanium and 0.0053 ± 0.0002 $Å^2$ for amorphous germanium.

The finite energy resolution of the monochromator decreases the amplitude of the EXAFS intereference function and will lead to coordination number smaller than the known values. However, by applying the energy resolution function, the coordination numbers can be corrected. Alternatively the coordination numbers can be obtained by comparing to reference compounds measured under the same operating conditions.

The laboratory can be developed further to obtain higher intensity x-rays, producing better quality EXAFS data as the result, by improving the bending crystal scheme, designing better detectors, and changing the x-ray source to a more powerful rotating anode source. The bending scheme used in the present work has a disadvantage: it causes defocusing of the beam in the vertical direction. This effect reduces the intensity by a factor of three. It also defocuses in the horizontal direction. The defocussing

effect broadens the energy resolution. A better bending scheme can be tried by cementing a crystal wafer to a backing plate which has a fixed radius [Khalid et al., 1982]. The energy resolution can be improved by decreasing the take-off angle. While we were unable to identify the source of the noise in the detector, it might be less noisy if the collecting plates and other conducting materials were made of the same metal. An ionization chamber built at SFU for fluorescent experiment at SSRL has smaller contact potentials and is less noisy (the noise level is one tenth of the present detectors). By replacing the present normal focus tube with a fine focus, the x-ray intensity can be increased. Also, a rotating anode source can increase the intensity by a factor of fifteen.

On the whole, the experiment/designing laboratory is good for learning/teaching EXAFS theory and practice. With the improvements suggested above, the facility can be used for preliminary experiments prior to going SSRL. Some experiments with concentrated materials, which do not demand high x-ray intensity, can also be done.

Appendix

Evaluation of a Focusing Monochromator

The energy resolution of a crystal monochromator depends on the geometrical precision and the size of the crystal, the widths of the anode image and receiving slit and the absorption coefficient of the crystal.

Various geometrical factors affecting the resolution of the resolution can basically be divided into three categories: horizontal and vertical broadening of the beam, and effects of the depth of penetration of the x-rays into the crystal.
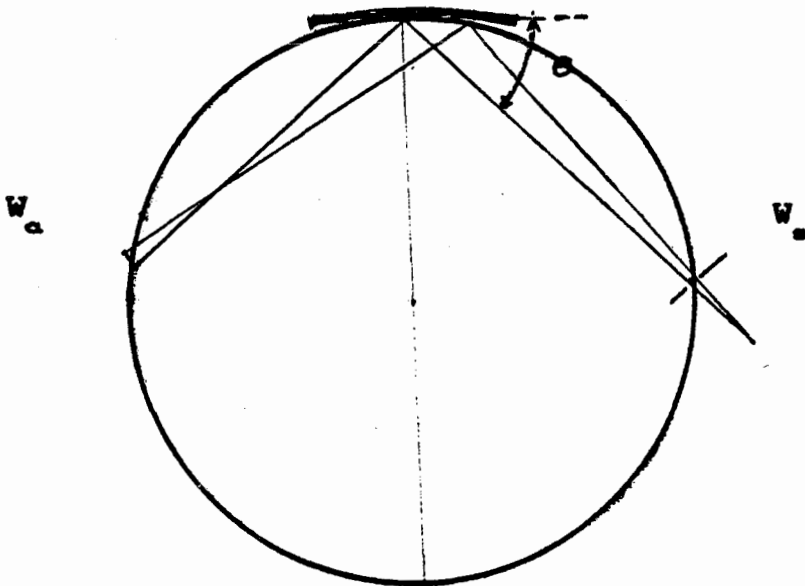
Fig. A.1: *Focusing arrangement.*

The maximum horizontal broadening is

$$\Delta\theta_H = \frac{W_s + W_a}{4R \sin \theta} , \qquad (A.1)$$

where W_s is the width of receiving slit, W_a is the projected width of the anode image and R is the Rowland circle (see Fig. A.1).

The vertical broadening is [Khalid et al., 1982]

$$\Delta\theta_v = \frac{h^2/2}{(4R \sin \theta)(4 R \cos \theta)} , \qquad (A.2)$$

where h is the height of the anode image.

The x-ray beams penetrate the crystal at the effective distance 2 $\ln(2)/\mu$, where μ is the linear absorption coeffient of the crystal. This penetration causes broadening: [Georgopoulos and Knapp, 1981]

$$\Delta\theta_P = \frac{2\ln(2) \cos \theta \cos \theta}{\mu \, 4 R \sin \theta} \qquad (A.3)$$

The maximum full width broadening can be calculated by combining (A.1), (A.2) and (A.3):

$$\Delta\theta = \frac{1}{4R \sin \theta} \{(W_{\alpha} + W_{s})^2 + (h^2/8R \cos \theta)^2 + (2\ln2 \cos \theta/\mu)^2\}^{1/2}$$

$$(A.4)$$

List of References

1. Agarwal, B. K., <u>X-Ray Spectroscopy</u>, Springer-Verlag, Berlin, 1979

2. Asheley, C. A. and Doniach, S., Phys. Rev., <u>B 11</u>, 1279, 1975

3. Bauchspiess, K. R. and Crozier, E. D., in <u>EXAFS and Near Edge Structure III</u>, edited by K. O. Hodgson, B. Hedman, and J. E. Penner-Hahn, Springer Proceeding in Physics, 2, Springer Verlag, Berlin, 1984, p. 514

4. Bienenstock, A., in <u>Laboratory EXAFS Facilities</u>, edited by E. A. Stern, AIP Conference Proceedings, 64, American Institute of Physics, New York, 1980, p. 150

5. Borchert, G. L., Hansen, P. G., Jonson, B., Ravn, H. L., Schult, O. W. B., and Tidemand-Petersson, P., Nucl. Instrum. Meth., <u>178</u>, 209, 1980

6. Bouldin, C. E. and Stern, E. A., in <u>EXAFS and Near Edge Structure III</u>, edited by K. O. Hodgson, B. Hedman, and J. E. Penner-Hahn, Springer Proceeding in Physics, 2, Springer Verlag, Berlin, 1984, p. 273

7. Brown, G. S. and Doniach S., in <u>Synchrotron Radiation Research</u>, edited by H. Winnick and S. Doniach, Chapter 10, Plenum, New York, 1980

8. Bunker, G., and Stern, E. A., Phys. Rev. Lett., <u>52</u>, 1990, 1984

9. Citrin, P. H., Eisenberger, P. and Kincaid, B. M., Phys. Rev. Lett., <u>36</u>, 1346, 1976

10. Clark, G. L., Applied X-Rays, McGraw-Hill Book Company, Inc., New York, 1955

11. Cohen, G. G., Fisher, D. A., Colbert, J., and Shevchik, N. J., Rev. Sci. Instrum., 51, 273, 1980

12. Cohen, G. G., and Deslattes, R. D., Nucl. Instrum. Meth. , 193, 33, 1982

13. Crane, E., in Laboratory EXAFS Facilities, edited by E. A. Stern, AIP Conference Proceedings, 64, American Institute of Physics, New York, 1980, p. 111

14. Crozier, E. D., Lytle, F. W., Sayers, D. E., and Stern, E. A., Can. J. Chem., 55, 1968, 1977

15. Crozier, E. D., and Seary, A. J., Can. J. Phys, 58, 1388, 1980

16. Crozier, E. D., and Seary, A. J., Can. J. Phys, 59, 876, 1981

17. Crozier, E. D., Rehr, J. J., and Ingalls, R. (1985), Amorphous and Liquid System, in X-ray Absorption: Principles, Techniques of EXAFS, SEXAFS and XANES, Chapter 9, Edited by R. Prins and D. C. Koningsberger, J. Wiley and Sons, Publisher, 1987

18. Cullity, B. D., Elements of X-ray Diffraction, Addison-Wesley Publishing Company, Inc., Massachusetts, 1978

19. DuMond, J. W. M., Rev. Sci. Instrum., 18, 626, 1947

20. DuMond, J. W. M., Lind, D. A., and Cohen, E. A., Rev. Sci. Instrum., 18, 617, 1947

21. Fisher, G.R., in Laboratory EXAFS Facilities, edited by E. A. Stern, AIP Conference Proceedings, 64, American Institute of Physics, New York, 1980, p. 21

22. Franks, A. and Breakwell, P. R., J. Appl. Crys., 7, 122, 1974

23. Elam, W. T., in <u>Laboratory EXAFS Facilities</u>, edited by E. A. Stern, AIP Conference Proceedings, 64, American Institute of Physics, New York, 1980, p. 51

24. Garbrielyan, K. T., Chukhovskii, F. N., and Pinsker, Z. G., Sov. Phys. Tech. Phys., <u>25</u>, 1, 1980

25. Georgopoulos, P., Sayers, D. E., Bunker, B., Elam, T. and Grote, W. A., in <u>Laboratory EXAFS Facilities</u>, edited by E. A. Stern, AIP Conference Proceedings, 64, American Institute of Physics, New York, 1980, p. 134

26. Georgopoulos, P., and Knapp, G. S., J. Appl. Cryst., <u>14</u>, 3, 1981

27. Goulon J., Goulon-Ginet, C., Cortes, R., and Dubois, J. M., J. Physique, <u>43</u>, 539, 1982

28. Hayes, T. M., Sen, P. N., and Hunter, S. H., J. Phys., <u>C 9</u>, 4357, 1976

29. Hayes, T. M. and Boyce,J. B., Solid State Physics, vol. <u>37</u>, edited by H. Ehrenreich et al., Academic Press, New York, 1982

30. Heald, S. M., in <u>Laboratory EXAFS Facilities</u>, edited by E. A. Stern, AIP Conference Proceedings, 64, American Institute of Physics, New York, 1980, p. 31

31. Ito, M. and Iwasaki, H., Jap. J. Appl. Phys., <u>22</u>, 347, 1983

32. Jaundrell-Thompson, F. and Ashworth, W. J., <u>X-ray Physics and Equipment</u>, F.A. Davis Company, Philadelphia, 1970

33. Kawasaki, T., and Udagawa, Y., Rev. Sci. Instrum., <u>54</u>, 1432, 1983

34. Khalid, S., Emrich, R., Dujari, R., Shultz, J. , and Katzer, J. R., Rev. Sci. Instrum., <u>53</u>, 22, 1982

35. Kincaid, B. M., _Synchrotron Radiation Studies of K-edge X-ray Photoabsorption Spectra: Theory and Experiment_, SSRP Report 75/03, Stanford University, Stanford, 1975

36. Knapp, G. S., Chen, H., Klippert, T. E., Rev. Sci. Instrum., $\underline{49}$, 1658, 1978

37. Lee, P. A., and Pendry, J. B., Phys. Rev., $\underline{B\ 11}$, 2795, 1975

38. Lee, P. A., Citrin, P. H., Eisenberger, P. , Kincaid, B. M., Rev. of Mod. Phys., $\underline{53}$, 769, 1981

39. Lengeler, B. and Eisenberger, P, Phys. Rev., $\underline{B\ 21}$, 4507, 1980

40. Lu, K. and Stern, E. A., in _Laboratory EXAFS Facilities_, edited by E. A. Stern, AIP Conference Proceedings, 64, American Institute of Physics, New York, 1980, p.104

41. Lytle, F. W., Sayers, D. E., Stern, E. A., Phys. Rev., $\underline{B\ \ 11}$, 4825, 1975

42. Maeda, H., Terauchi, H., Tanabe K., Kamijo, N., Hida, M., Kawamura, H., Jap. J. Appl. Phys., $\underline{21}$, 1342, 1982

43. Morgan, K. Z., in _American Institute of Physics Handbook_, edited by D. E. Gray et al., McGraw-Hill Book Company, Inc., New York, 1963, p. 8-312

44. Muller, J. E. and Schaich, W. L., Phys. Rev., $\underline{B\ 27}$, 6489, 1983

45. Sandstrom, D. R. and Fine, J. M., in _Laboratory EXAFS Facilities_, edited by E. A. Stern, AIP Conference Proceedings, 64, American Institute of Physics, New York, 1980, p. 127

46. Sayers, D. E., Stern, E. A. and Lytle, S. W., Phys. Rev. Lett., $\underline{27}$, 1204, 1971

47. Schaich, W. L., in <u>EXAFS and Near Edge Structure III</u>, edited by K. O. Hodgson, B. Hedman, and J. E. Penner-Hahn, Springer Proceeding in Physics, 2, Springer-Verlag, Berlin, 1984, p. 2

48. Seary, A. J, 1987 (private communication)

49. Stern, E. A., Phys. Rev., <u>B 10</u>, 3027, 1974

50. Stern, E. A., Sayers, D. E., and Lytle, Phys. Rev., <u>B 11</u>, 4836, 1975

51. Stern, E. A., in <u>Laboratory EXAFS Facilities</u>, edited by E. A. Stern, AIP Conference Proceedings, 64, American Institute of Physics, New York, 1980, p. 39

52. Stern, E. A., in <u>Laboratory EXAFS Facilities</u>, edited by E. A. Stern, AIP Conference Proceedings, 64, American Institute of Physics, New York, 1980, p. 160

53. Stern, E. A., and Kim, A., Phys. Rev., <u>B 23</u>, 3781, 1981

54. Stern, E. A., in <u>EXAFS for Inorganic Systems</u>, edited by C. D. Garner and S. S. Hasnain, Science and Engineering Research Council, Daresbury Laboratory, England, 1981, p. 40

55. Templeton, T., 1986 (private communication)

56. Teo, B. K., and Lee, P. A., J. Am. Chem. Soc., <u>101</u>, 2815, 1979

57. Thulke, W., Haensel, R., and Rabe, P., Rev. Sci. Instrum., <u>54</u>, 1983

58. Tohji, K., and Udagawa, Y., Jap. J. Appl. Phys., <u>22</u>, 882, 1983

59. Webb, N. G., Rev. Sci. Instrum., <u>47</u>, 545, 1976

60. White, J. E, J. Appl. Phys., <u>21</u>, 855, 1950

61. Wilkinson, D. H., <u>Ionization Chambers and Counters</u>, University Press, Cambridge, 1950

62. Williams, A., Rev. Sci. Instrum., $\underline{54}$, 193, 1983

63. Winnick, H. , in Synchrotron Radiation Research, edited by H. Winnick and S. Doniach, Chapter 2, Plenum, New York, 1980

64. Witz, J., Acta Cryst., $\underline{A25}$, 30, 1969

65. Zschornack, G., Muller, G., and Musiol, G., Nucl. Instrum. Meth., $\underline{200}$, 481, 1982